SlimVar: rapid *in vivo* single-molecule tracking of chromatin regulators in plants

Alex L. Payne-Dwyer[1,2], Geng-Jen Jang[3], Caroline Dean[3], and Mark C. Leake[1,2]*

[1] School of Physics, Engineering and Technology, University of York, YO10 5DD, UK.

[2] Department of Biology, University of York, YO10 5DD, UK.

[3] Cell and Developmental Biology, John Innes Centre, Norwich Research Park, NR4 7UH, UK.

*Correspondence: mark.leake@york.ac.uk

Abstract

Epigenetic regulation occurs over many rounds of cell division in higher organisms. However, visualisation of the regulators *in vivo* is limited by imaging dynamic molecules deep in tissue. We report new technology—Variable-angle Slimfield microscopy (SlimVar)—that enables tracking of single fluorescent reporters to 30 µm depth through multiple *Arabidopsis thaliana* root tip cell layers. SlimVar uses rapid photobleaching to resolve tracked particles to molecular steps in intensity. By modifying widefield microscopy to minimise optical aberrations and robustly post-process few-photon signals, SlimVar mitigates performance losses at depth. We use SlimVar to quantify chromatin-protein assemblies in nuclei, finding that two homologous proteins key to epigenetic switching at *FLOWERING LOCUS C* (*FLC*) —cold-induced VERNALISATION INSENSITIVE3 (VIN3) and constitutively expressed VERNALISATION 5 (VRN5)—exhibit dynamic assemblies during *FLC* silencing. Upon cold exposure, the number of assembly molecules increases up to 100% to a median of ~20 molecules. Larger VRN5 assemblies preferentially colocalise with an *FLC lacO* transgenic reporter during prolonged cold and persist after return to warmth. Our findings support a hybrid model of epigenetic memory in which nucleation of histone trimethylation is assisted by dynamic protein assemblies over extended durations. SlimVar offers molecular insights into proteins expressed at physiological levels in tissues.

Introduction

Understanding the basis of epigenetic silencing remains a major question, with potential implications for both novel medical therapeutics [1] and agricultural biotechnology [2]. It is not yet known how cells process delocalised, long-term sensory information into genetic states that are stable enough to facilitate not only cellular differentiation but also determine key organism-level transitions, including those relevant to medicine such as ageing and disease [3]. Similarly, mysteries remain regarding long-term epigenetic responses to key environmental cues, including seasonal temperature fluctuations, govern the productivity and resilience of crops to challenges such as climate change [4].

A key conserved epigenetic mechanism across eukaryotes - including humans and plants - is Polycomb-mediated silencing [5], which involves modification of trimethylated histone H3 lysine 27 (H3K27me3). H3K27me3 initially accumulates at a nucleation site then spreads

across a locus to stably maintain a silenced state through many rounds of cell division [6,7]. Polycomb Repressive Complex 2 (PRC2) silencing has been well studied in *Arabidopsis* gene *FLOWERING LOCUS C* (*FLC*) [8]. *FLC* encodes a repressor of flowering and is epigenetically silenced during a process called vernalisation by the prolonged cold of winter; lowering repressor levels enables flowering in spring [9–11]. Cold exposure increases the probability that each *FLC* locus will epigenetically switch from ON to OFF states through nucleation of H3K27me3 at an intragenic site [12,13]. Upon return to warm conditions, H3K27me3 spreads across the locus to give long-term stable silencing [14]. What has been less clear is how the relative stability of the nucleated state is inherited following cell division. Each nucleation event involves only three nucleosomes, too few to survive random replicative dilution through the classic Polycomb 'read-write' mechanism [11,15,16]. Metastable protein assemblies have been proposed to explain the inheritance of the nucleated state [17]. PRC2 accessory proteins are thought to restore the stochastic loss of histone marks by stimulating Polycomb Repressive Complex 2 (PRC2) activity [18]. While individual proteins may only interact transiently with nucleation factors and the locus, a recent model predicts that an assembly - with the appropriate positive cooperativity – can become dynamically self-sustaining above a threshold number of recruited proteins [17]. In this framework, a sufficiently large assembly of proteins could act as a binary memory element working together with established H3K27me3 machinery at a given locus. This model highlights molecule number as a key factor.

Two PRC2 accessory proteins required for stable cold-induced silencing at *FLC*, VERNALISATION INSENSITIVE3 (VIN3) and VERNALISATION 5 (VRN5, also known as VIN3-LIKE 1 / VIL1), expressed in shoot and root tips are clear candidates for this form of memory storage [19]. VIN3 and VRN5 (collectively called VEL proteins) associate with the PRC2 complex and with the *FLC* nucleation region that accumulates H3K27me3 specifically during cold conditions [11,20]. At <15°C, *VIN3* expression gradually rises over several weeks, while in warm conditions >15°C, expression decays rapidly within approximately 4 h [9,10,20]. VIN3 and its assemblies could therefore in principle report the duration of cold conditions during winter to promote an epigenetic switch. However, due to its instability in the warm, one or more additional factors—a promising candidate being VRN5—are required at the *FLC* nucleation region to explain persistent memory of silencing following a change to warm conditions. Both VIN3 and VRN5 contain complex plant homeodomains (PHDs) [19] which do not interact directly with histone tails [21], FNIII domains and C-terminal VEL domains [22,23]. Of these three domains common to VIN3 and VRN5, the VEL domain mediates head-to-tail interactions. VEL proteins that oligomerise and even form phase-separated droplets under transient overexpression are directly associated with stable silencing at *FLC* [23]. A key question is then: do physiological levels of VIN3 and VRN5 oligomerise sufficiently in the vicinity of *FLC* during vernalisation, to fulfil this model?

Here, we describe development of an efficient new technology, Slimfield Variable Angle (SlimVar), and apply it to rapidly track and quantify VEL proteins in live plant tissue. Prior investigation of nuclear oligomers has been constrained by an inability to detect individual,

rapidly diffusing protein molecules deep within plant tissue. Traditional confocal [24], structured illumination [25] and lightsheet microscopy [26] lack the required combination of sensitivity and speed for single-molecule tracking in live plants, which remains a challenge beyond the first cell layer [27–34]. Although complex, expensive super-resolution methods including lattice lightsheet [35,36] and MINFLUX [37,38] are in principle capable of deeper imaging, to date neither has been successfully applied at a molecular scale in plants. In addition, these require both specialised hardware and/or photoactivatable/photoswitchable fluorescent proteins [39,40] or dyes [41,42].

SlimVar, instead uses common fluorescent protein fusions in existing transgenic plants without requiring overexpression, as well as a relatively accessible microscope platform compared to other single molecule techniques. Adapted from Slimfield microscopy,[43–45] SlimVar uses a grazing angle of incidence optimised for observing single nuclei up to approximately 30 µm deep in root tissue, while tracking single fluorescent protein molecules at up to 40 nm lateral spatial precision. Whereas Slimfield has been limited to simple unicellular samples or the surfaces of *ex vivo* tissue sections [46], SlimVar enhances the image contrast and mitigates optical aberrations at depth to enable dynamic spatial localisation in complex multicellular samples. The use of root tips confers optical advantages of lower autofluorescence and more regular, less refractive layers than other plant tissues. Single-molecule sensitivity is combined with stepwise photobleaching analysis [43] to quantify the number of molecules in any observed oligomeric assemblies. This sensitivity simplifies the use of transgenic plant lines expressing from as few as a single gene copy and enables imaging of physiological states of low-abundance nuclear proteins.

We first introduce the principles and operational procedures of SlimVar, and demonstrate its measurement capabilities. Applying to it root tips, we find that both VIN3 and VRN5 proteins form assemblies in cell nuclei, composed of consistent dimeric subunits. In lines expressing from single-digit exogenous copies of VIN3 and VRN5, the median assembly comprises up to ~20 molecules of each protein, in agreement with that required for protein memory elements predicted from modelling [17]. We also use an *FLC-lacO*/LacI-YFP transgenic reporter to localise the *FLC* locus and characterise its mobility relative to VEL proteins. Finally, we demonstrate dual-colour SlimVar, which directly shows VRN5 assemblies present at *FLC*. We find that larger VRN5 assemblies preferentially colocalise with *FLC* after long cold exposure and after return to warm conditions, and that this interaction between individual larger oligomers of VRN5 and *FLC* is dynamic on a sub-second timescale.

Results

SlimVar enables molecular quantification of diffusing particles deep in tissue

SlimVar is a 2D + time imaging technique which identifies fluorescent **foci** from local intensity maxima in each video frame (Fig. 1, Table 1). Foci correspond to at least one, or more generally, of a localised group of labelled molecules much smaller than the widefield resolution limit; output parameters include 2D spatial location, total intensity in photons, and **signal-to-noise ratio** (SNR). If the frame rate is rapid enough to overcome motion blur, foci from sequential frames can be linked into **tracks**. Since the molecules in a track are spatially correlated we can infer that they form an intermolecular **assembly**, and that each track corresponds to one assembly.

Rapid tracking of single diffusive proteins requires minimal background (equivalent to $<10^7$ photons per $\mu m^2/s$), and a photon-sensitive, low-noise detector (<2 electrons readout per pixel) with millisecond or less sampling. Maximising the emissive output of fluorescent protein tags in these short exposures requires high excitation intensity (~kW/cm^2).

Photobleaching dominates under these conditions, which SlimVar uses to capture the emission intensities of both

i) the initial unbleached state of each assembly, and
ii) its constituent single fluorophores,

in the same short (~10 s) acquisition.

The ratio of these—**stoichiometry**—is an estimate of the number of molecules in each assembly. The numerator in this ratio is the track's initial intensity; its relative uncertainty is low since the first of its foci contains many photons. The uncertainty can be reduced further by interpolation from fitting the photobleach trend in time.

The denominator in the ratio relates to single molecule detection events, each containing few photons; there may be very few or no such events that can be associated with a particular assembly, for example if it leaves the detection volume. Instead, we consider the population-average number of photons associated with each fluorophore—the **characteristic molecular brightness.** It can be determined by averaging the height of individual photobleaching steps [43] (Supplementary Fig. 1). As an average, it is only a reliable estimate for individual assemblies if the intensities are narrowly distributed for fluorophores of the same type in the same environment, and independent of concentration. These conditions are well satisfied by intracellular fluorescent protein fusion constructs, which do not easily self-quench [47,48]. These intensities represent photons per frame and, if not in a saturating regime for emission, scale with the exposure time, excitation power and the photon collection efficiency of the microscope. However, the characteristic molecular brightness can be internally calibrated within each sample or dataset for a ~20 µm range of working depths. For this reason, it is best practice to acquire additional frames until an excess of independent single-molecule events has been accrued.

It is possible to estimate stoichiometry by counting photobleaching steps directly,[49] but this strategy is typically limited to roughly <10 steps per track due to increasing likelihood of stochastic missing/overlapping steps for higher stoichiometry assemblies. Our ratiometric method instead estimates the stoichiometry of tracks which begin close to the start of the acquisition, typically within a quarter of a photobleaching decay time or less, thus

containing minimal prior photobleached content. This approach enables accurate counting over a broader range of stoichiometries than direct step detection.

Independent of the tracking pipeline, SlimVar can quantify the **total protein number** in the detection volume, or sub-region such as a section of the cell nucleus. We sum all the initial pixel intensities (measured as number of photons) in segmented region of each image and normalise these values by the characteristic brightness corresponding to a single fluorescent dye tag. We define the total protein number as the difference in mean integrated intensity between the test population and that of the unlabelled negative control to corrected for any autofluorescence. We interpret this as the average number of labelled molecules in the volume. It is a reliable population-level measure of protein content and concentration.[45]

Since each assembly is associated with a sequence of discontinuous steps along its track, we also quantify the assembly's mean **diffusivity** using mean-square displacement analysis (Methods). While photobleaching shortens the average track, it transiently improves the optical contrast which is ideal for rapid, high-content tracking. The diffusivity can be used to determine if the assembly is immobile on the timescale of the experiment and therefore likely to be bound, for example to chromatin.

In multicolour SlimVar, multiple channels are captured and tracked independently from the same acquisition. Once the two channels are spatially coaligned, the tracks' spatial and temporal coordinates are compared. This enables measurement of dynamic **colocalisation** of pairs of tracked particles such as different types of protein that are labelled with different colour dyes. This is a powerful correlative approach which can test the dependence of colocalisation on metrics associated with each assembly, such as stoichiometry and diffusivity.

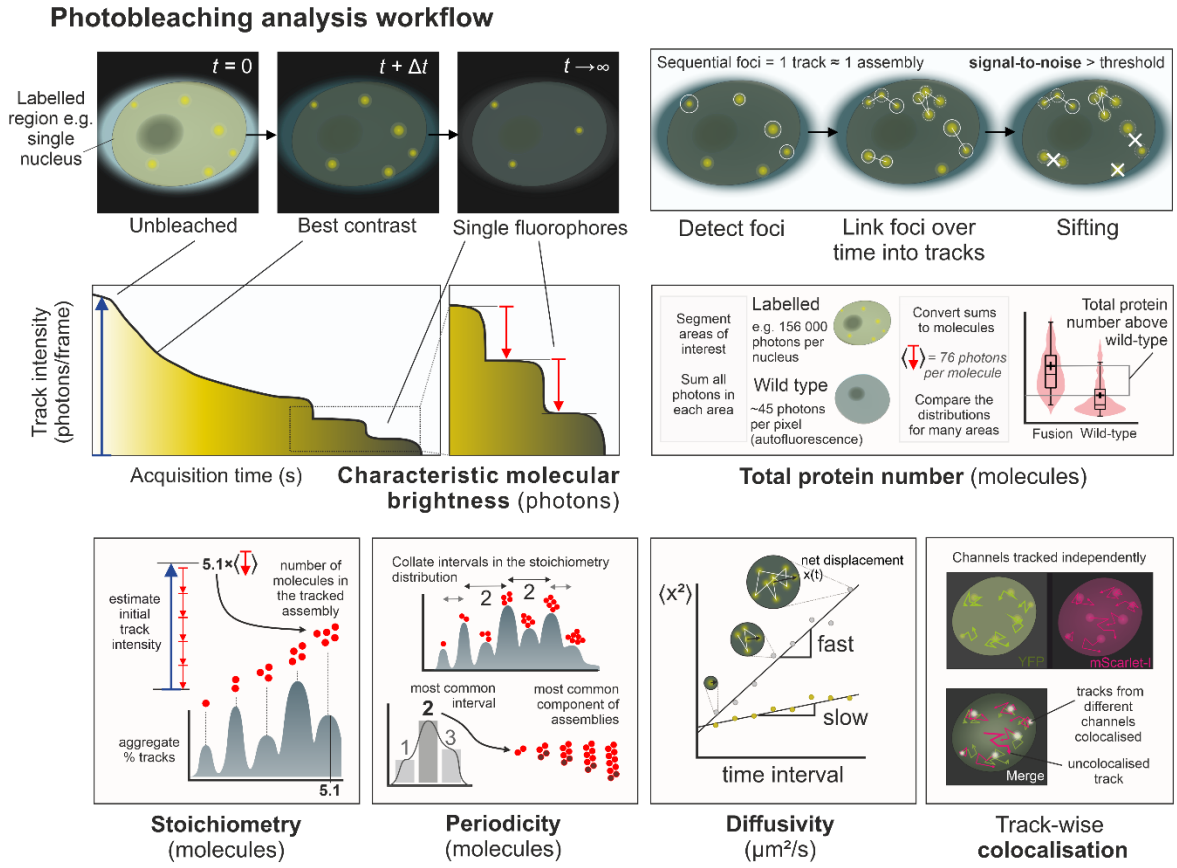

Fig. 1. Correlative quantification of diffusing assemblies using SlimVar. Terms are defined in Table 1. SlimVar delivers a) rapid photobleaching in image sequences at high framerate to outpace molecular diffusion, followed by b) robust postprocessing and quality control steps to identify foci in individual frames, and tracks across multiple (up to 20) frames, which correspond in general to assemblies of labelled molecules. c) The full extent of photobleaching enables estimates of the characteristic molecular brightness, which is narrowly distributed for a fluorescent protein. The characteristic molecular brightness is used to determine d) total protein number for each region of interest and e) stoichiometry for each tracked assembly near the start of the image sequence, as number of molecules. These metrics are corrected for autofluorescence using unlabelled wild type then collated over a population, enabling robust estimation for average total protein number. f) Periodicity analysis extracts patterns from the stoichiometry distribution to infer consistent repeat units of assemblies. g) Rapid tracking facilitates mean-square displacement analysis to estimate individual assembly mobility. h) Multicolour SlimVar assesses whether stoichiometry and diffusivity are dependent on colocalisation between different pairs of assemblies.

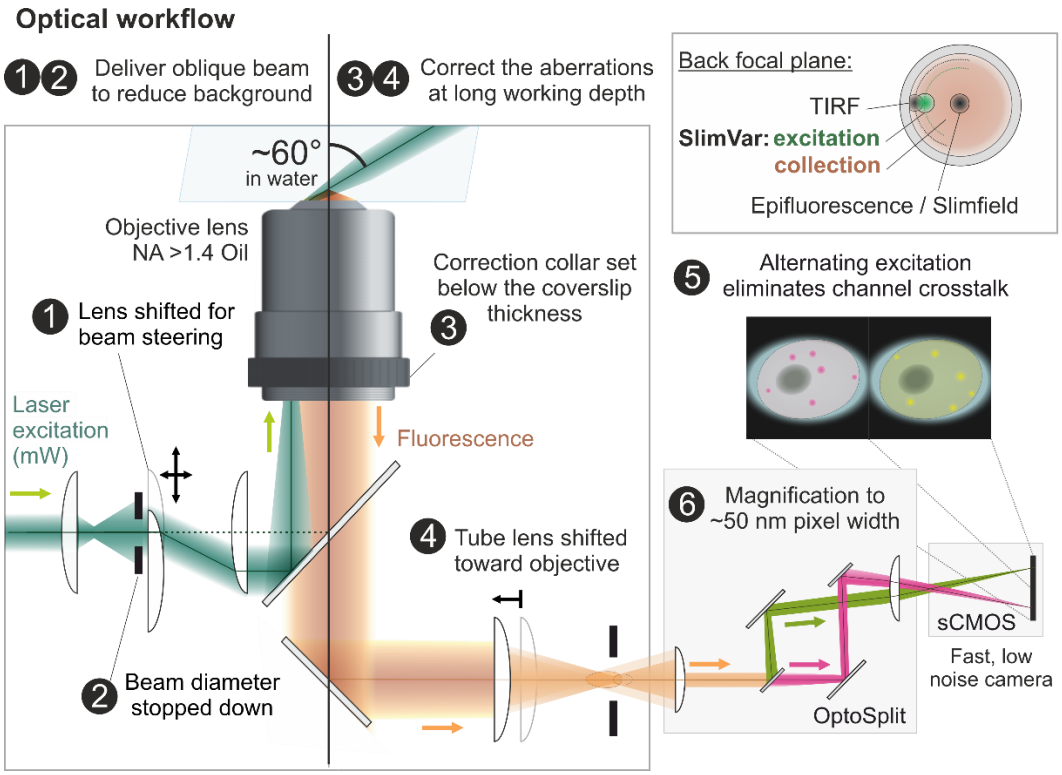

Fig. 2. SlimVar enhances optical contrast at greater working depths. The optical scheme for SlimVar adapts widefield or objective-based TIRF (total internal reflection fluorescence) microscopy capable of detecting single molecules at a coverslip surface, and extends this to greater working depths. A narrow, collimated excitation beam is delivered at a steep but subcritical angle by (1) adjusting the position of a steering lens. The intersection of the focal plane and excitation beam defines a sub-micron high detection volume at the set working depth. The lateral size of this volume can be (2) adjusted using an iris or beam stop to match sample dimensions and reduce background. Aberrations, inherent to oil immersion lenses at depth, are mitigated at the set working depth using a calibration procedure. Either a test sample or an *in vitro* beads-in-agarose phantom may be used. This comprises a combination of adjustments to (3) an objective lens correction collar and, where necessary, (4) shifting the tube lens towards the objective. The microscope uses a single detector with two colour channel splitter (Cairn OptoSplit); note, the beam is not stopped down after entering the splitter and is shown here with a narrowed diameter only for clarity. In multicolour experiments, contrast is protected from channel crosstalk by (5) alternating excitation wavelengths between subsequent frames. The second pair of lenses in the detection path provides (6) additional magnification (1.2–2.2× depending on physical sensor pixel size) to ensure the point spread function (PSF) is spatially oversampled for super-resolved localisations.

Implementation of single-molecule photobleaching analysis requires the maximum optical contrast, while maintaining both sampling rate and signal-to-noise sufficient to detect foci. The widefield configuration (Fig. 2) maximises fluorescence emission collection from foci within each detection volume. It uses the full back aperture of the objective lens and a minimal number of optical components in the detection path. SlimVar adjusts these

elements to mitigate loss of optical contrast at high working depths. These adjustments address either the fluorescence excitation, or the aberrations (blurring of static objects) in the emission path.

The optimal excitation intensity is a few kW/cm^2 (~10 mW total power within a beam of approximately 25 µm diameter) which maximises fluorescence emission, whilst being sub-saturating for the dyes and ensuring photobleaching is not too rapid relative to the sampling time. The contrast can be further improved by minimising out-of-focus background. SlimVar avoids exciting the sample outside the detection volume by employing a narrow beam of near-collimated illumination delivered at an oblique-angle similar to variable angle epifluorescence microscopy (VAEM) [50] and highly inclined illumination (HILO) [51,52]. The excitation laser(s) are coaligned and focused into the back focal plane of the high numerical aperture objective lens. To progressively tilt the beam in the sample, this focus is moved to a precise lateral displacement from the optic axis using a steering lens (Fig. 2, point 1) placed conjugate to the back focal plane. The maximum shift of ~3 mm radius would generate a large tilt for TIRF) excitation (Fig. 2, inset); for SlimVar, the beam is instead shifted by 2.3 ± 0.2 mm corresponding to a free beam tilted to 60 ± 5 ^{o} at the sample, subcritical for TIRF. The beam is then stopped down to match the sample dimensions (Fig. 2, point 2) which eliminates further background unrelated to the region of interest.

At low working depths, aberrations in the emission path are corrected by design for most high numerical aperture lenses. However, scattering and aberrations emerge at higher working depths; of these, the most detrimental is spherical aberration caused by differences in refractive index between the immersion medium and the aqueous sample, that compounds rapidly with additional working depth. While in principle SlimVar admits the use of water immersion lenses (NA < 1.3) that minimise this effect, here we adapt the widefield microscope to make more efficient use of a higher numerical aperture oil immersion objective lens with a correction collar (NA = 1.49). These adaptations compensate the optical aberrations at a desired working depth. Using a precision microscope stage, the working depth is set by difference from the axial position where the coverslip surface appears in focus. We present a **calibration procedure**, inspired by previous works improving optical trapping[53–55] or imaging [56,57] using high numerical aperture in aqueous samples. It adjusts the optical pathway—including beam collimation, objective correction collar setting and tube lens position—to minimise aberrations at a representative depth of 25 µm (Fig. 2, points 3-4). This calibration improves the optical contrast sufficiently for imaging and tracking across the range of working depths up to 30 µm (Supplementary Figs. 2 and 3). This procedure can be performed either with a live root sample resting on the coverslip, or a phantom using beads suspended in agarose (Methods). We assessed the improved optical contrast using the width of the point spread functions (PSFs) (Supplementary Fig. 3) and quantified an effective numerical aperture of 1.38 ± 0.02, which though reduced from the diffraction-limited performance, still exceeds that of a water immersion objective lens. Both axial and lateral resolution are improved for beads, and the severe loss of axial performance associated with depth is mitigated in plant roots.

For multicolour experiments, multiple continuous wave lasers are spatially filtered and expanded to the same dimensions, then coaligned using dichroic mirror beamsplitters.

Crosstalk and bleed-through effects tend to decrease the contrast or introduce ambiguous signals; to avoid this we excite and subsequently analyse each channel in alternating interleaved frames (Fig. 2, point 5). This proportionally decreases the effective sampling rate but otherwise maintains the tracking performance of single-colour imaging.

Spatial oversampling—a small pixel size relative to the widefield spatial resolution—is necessary for postprocessing. It is introduced by additional magnification in the detection path (Fig. 2, point 6). Although each signal is spread more thinly over a greater number of pixels, the lower chance of spurious correlations makes detection more robust to variations in foci shape due to defocus or motion. Oversampling also ensures the localisation precision is not limited by pixel size.

To mitigate detrimental effects of background noise and spatial overlap on the final metrics, **sifting** is performed to only accept tracks above a minimum set signal-to-noise ratio and track length. Using a dedicated single molecule assay *in vitro* (Supplementary Fig. 2a-b) and our tracking data from live plants, we found appropriate sifting thresholds determined by two factors: detector noise (Supplementary Fig. 2c) and autofluorescence relative to the probe's characteristic molecular brightness (Supplementary Fig. 4). Sifted tracks have a positive predictive value >95% for single YFPs *in vitro* (Supplementary Fig. 2d) and >90% for YFP-labelled assemblies in plant roots (Supplementary Fig. 2e).

We assessed the combined improvements to optical and sifting performance using the characteristic molecular brightness of the fluorophore and the total number of photons collected per track. The increase in apparent characteristic molecular brightness with excitation power (Supplementary Fig. 2f), indicates that the detected photon flux associated with single molecule detection at 25 µm depth *in vitro* is only >50 photons per frame, and therefore >150 photons per single molecule track. Our practical values for characteristic molecular brightness fall in the range 70-200 photons per frame. The total flux emitted is much larger (~1,000 photons/ms), with many photons producing the raw image but fewer photons captured in tracks. This is further illustrated by comparing the numbers of photons per track for *in vitro* control and *in vivo* data (Supplementary Fig. 2g-h). Modes of 190–400 photons per single molecule track are observed, up to a maximum of ~5,000 photons per single molecule. This accounts for ~5% of a typical single fluorescent protein molecule budget of 10^5 photons [58,59]. This net transmittance corresponds reasonably well to the expected 10%, accumulated from transmittance of the sample (~80% in agarose, ~60% in root tips), effective numerical aperture (29% solid angle), detection optics (~60%) and detector (fill factor >99%, quantum efficiency ~92%). Most tracks have a photon total an order of magnitude lower, primarily due to the truncating effect of photobleaching (which is accelerated at the high excitation irradiance required), or simply by diffusion out of the detection volume. So, while the observed photon counts *in vivo* are low compared to theoretical limits of photon budgets for bright fluorescent proteins, they are reasonable considering a realistic budget subject to diffusive, photobleaching and scattering losses.

The fastest diffusivity that SlimVar can detect lies in the range 5–30 $\mu m/s^2$ depending on sampling rate. Only single proteins, if any, exhibit this diffusivity in an intracellular context, and these can still be inferred from the total protein number. Importantly, this suggests that oligomeric assemblies and associated metrics remain representative of the underlying

320 population through sifting, even in cases where the direct detection rate of single molecules
321 is reduced, or where the tracks are truncated. Subject to these limitations, SlimVar is
322 therefore suitable not only for detecting single molecules in plant tissues but also counting
323 molecules within assemblies (stoichiometry and periodicity), and measuring their mobility
324 (diffusivity) and interactions (colocalisation) simultaneously.

325

326 SlimVar resolves dynamic single assemblies of VIN3 and VRN5 in plant nuclei

327 For examining VIN3 and VRN5 protein localisation and self-assembly behaviours, during and
328 after cold treatment, we utilised lines with VIN3-EGFP/*vin3-4 FRI* [11,60] or VRN5-EYFP*/vrn5-8*
329 *JU223* [11,19] (referred to as VIN3-GFP and VRN5-YFP respectively) with variable transgene
330 copy numbers among progeny due to genetic segregation. To investigate the effects of
331 protein expression and to exploit greater imaging contrast and lower autofluorescence
332 associated with yellow and red fluorophores, we later also characterised new lines
333 containing VIN3-SYFP2/Col*FRI* (Supplementary Fig. 5) or VRN5-mScarlet-I/*vrn5-8 FRI*
334 (Supplementary Fig. 6) with different numbers of transgenes. These lines include active *FRI*
335 alleles so require effective vernalisation for flowering [20].

336 As a benchmark, we performed traditional confocal microscopy imaging on whole roots (Fig.
337 3a) with typical sampling at 35 s per frame (Fig. 3b and Supplementary Fig. 7). After
338 identifying nuclei from transmitted light images, we found that both VIN3 and VRN5
339 exhibited bright but largely diffuse fluorescence localised to the nucleoplasm. We
340 determined the qualitative autofluorescence from the Col*FRI* negative control; the
341 autofluorescence is greater under 488 nm wavelength excitation but this line shows no
342 signal localisation in either channel (Supplementary Fig. 7). While VRN5 was detectable
343 above this unlabelled background in all nuclei (N=241) at all timepoints, VIN3 is only
344 discernible during the cold period itself. Its total brightness in nuclei decreased at
345 subsequent timepoints after this, being undetectable within one week after return to warm
346 conditions, as reported previously [10]. During cold, the VIN3 signal per cell was initially
347 greatest in the vicinity of the meristem and epidermis, before becoming brighter in all cells
348 after further cold exposure (Supplementary Fig. 7).

349 We then performed Airyscan, an enhanced form of confocal laser scanning microscopy
350 which uses a point detector array; after optimising the point dwell time, field of view and
351 laser irradiance, we obtained faster frame sampling times down to 60 ms for individual root
352 tip nuclei enabling attempts at video tracking [61]. These image sequences showed a
353 marginally more granular spatial patterning than standard confocal microscopy, hinting at
354 the presence of distinct foci within the diffusive fluorescence (Fig. 3c), with residence times
355 in a similar range to the sampling time (Fig. 3d).

356

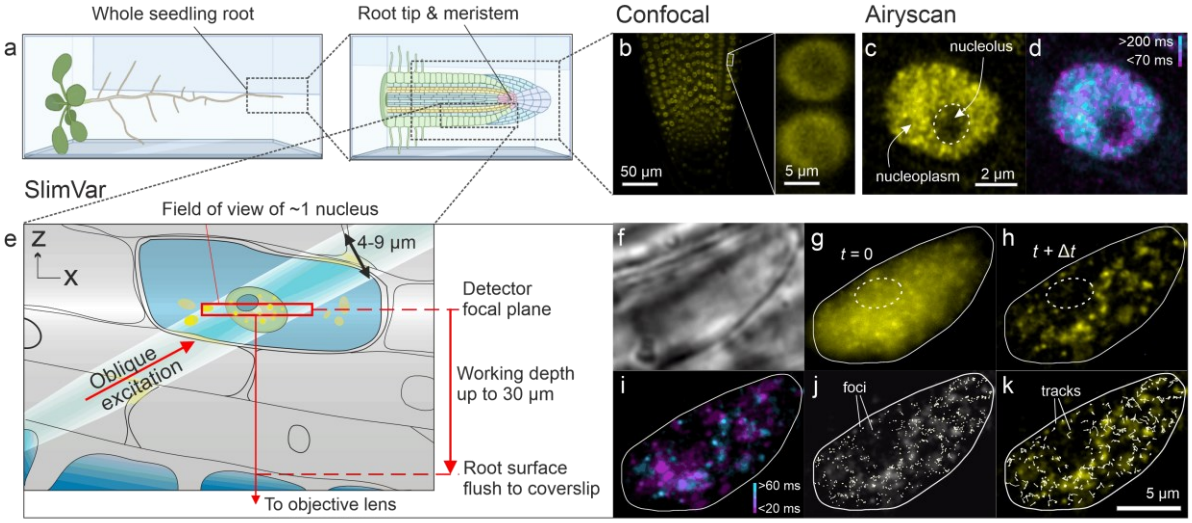

Fig. 3. SlimVar resolves dynamics of VIN3 and VRN5 assemblies during cold exposure of root tips. a) Whole roots mounted horizontally in aqueous media between agarose and coverslip, suitable for confocal and SlimVar microscopy. b) Projections of confocal z-stacks of root tips after 6 weeks of cold with VRN5-YFP reporter; acquisition time 35 s. Insets (interpolated) show labelled protein signals consistently localised to the nucleoplasm but not the nucleolus. Nuclear patterning of VEL proteins (c.f. confocal images in Supplementary Fig. 7) was typically round or lens-shaped, with a median length 7.8 µm (interquartile range IQR: 5.7–10.3 µm, N=571), and aspect ratio of 1.16 (IQR: 1.06–2.10), comparable to other nuclear reporters [62]. c,d) Airyscan images of VRN5-YFP after 2 weeks' cold indicating heterogeneous spatial distribution; c) maximum intensity projection of three *z*-slices, averaged over three consecutive timepoints; d) residence times over the same timepoints estimated from ratio between median and standard deviation of pixel values across the three frames. Low standard deviation (cyan) indicates low foci displacement over the three frames (200 ms) equivalent to diffusivity <0.1 $\mu m^2/s$, while high standard deviation (magenta) indicates high displacement over 70 ms, or diffusivity >0.3 $\mu m^2/s$. e) Schematic indicating illumination and detection volumes and working depth specific to SlimVar of root tip nuclei. f-k) SlimVar images of a root tip labelled at VRN5-YFP before vernalisation. f) Brightfield, used to identify nuclei in the field of view; g) initial frame in YFP channel prior to photobleaching, with nucleolus indicated (white dashes) showing background of overlapping signals; h) early stage photobleaching revealing distinct assemblies due to transient increase in background contrast (mean projection of frames 4–6); i) SlimVar resolves assemblies of differential mobility on ms timescales shown here as distinct slow- (cyan, >60 ms residence time, diffusivity <0.4 $\mu m^2/s$) and fast-moving (magenta, <20 ms residence time, diffusivity >1.4 $\mu m^2/s$) objects, represented by pixelwise ratio of median and standard deviation projections over three frames. j) Foci are detected from local maxima to super-resolved localisation precision. All sifted foci (Methods) for full sequence shown superimposed (white circles) on image from panel h (greyscale); k) tracks, generated by linking similar nearby foci, indicate individual assemblies with independent estimates of

388 stoichiometry and diffusivity. All sifted tracks from entire sequence shown superimposed
389 on image from panel with one vertex per timepoint (white arrows).
390
391 We then implemented SlimVar (Fig. 3e-k) capable of single-molecule fluorescent protein
392 detection at sub-ms levels, by first identifying nuclei in brightfield (Fig. 3f) to avoid
393 premature photobleaching. We found qualitatively similar nucleoplasmic morphology and
394 localisation (Fig. 3g), but instead of diffuse fluorescence we observed multiple, highly
395 mobile, distinct particles (Fig. 3h) with residence times longer than the exposures,
396 consistent with a sensitivity and sampling speed sufficient to overcome motion blur (Fig. 3i).
397 We thereby detected protein assemblies as distinct foci (Fig. 3j) and connected them into
398 tracks (Fig. 3k).
399 The excitation beam encapsulates individual cell nuclei between 4–16 µm wide but with
400 minimal excitation of the remaining >70% of the cell volume. It is ideally aligned for the
401 target root tip cells in at least three surface cell layers overlaying the stem cell niche (Fig. 3a
402 and Supplementary Fig. 8), with associated reduction in aberration, backscatter and out-of-
403 focus fluorescence excitation of intermediate cell layers. The contrast available for imaging
404 and tracking indicates that, in principle, cells of different types can be quantitatively
405 discriminated. While SlimVar does not fully recover diffraction-limited resolution in images
406 (Supplementary Fig. 3), the net result is an improvement in our signal-to-noise metric for
407 tracking VRN5 fluorescent reporters in assemblies by a factor of ~2.6 relative to
408 epifluorescence microscopy, including adjustment for the faster exposures (Supplementary
409 Fig. 2i, Methods). The capability for single-molecule detection is comparable with control
410 samples of purified fluorescent protein (Supplementary Fig. 2). The characteristic molecular
411 brightness is sufficiently consistent across the range of working depths to collate
412 acquisitions for each line.
413

414 Vernalisation induces upregulation and self-assembly of VIN3 and VRN5

415 The visual changes in VIN3 and VRN5 fluorescence during cold exposure suggest
416 corresponding changes in nuclear expression. To test this quantitatively, we acquired
417 SlimVar datasets from nuclei in VRN5-YFP and VIN3-GFP lines. From these, we first
418 determined the characteristic molecular brightness for the GFP and YFP tags (Methods,
419 Supplementary Fig. 1). As a negative control, we imaged nuclei in the Col*FRI* line using the
420 same 488 nm and 514 nm wavelength excitation modes (Supplementary Fig. 4). We then
421 estimated the total protein numbers in each nucleus of VRN5-YFP and VIN3-GFP (Fig. 4a).
422 VRN5 was highly abundant at all timepoints, with levels an order of magnitude greater than
423 VIN3 in the VIN3-labelled lines (Fig. 4a). Total VRN5 approximately doubles in response to
424 full vernalisation and persists after return to warm conditions. Total protein numbers
425 translate to nucleoplasmic concentrations of ~100 nM–1 µM for VIN3 and 1–10 µM for
426 VRN5 (Methods). When applied to the cell cytoplasm, the high sensitivity of SlimVar was
427 also able to establish that the fluorescence signals for both VIN3 and VRN5 were marginally
428 above Col*FRI* negative control levels, equivalent to a concentration at least 10,000-fold less
429 than those measured in the nucleus.

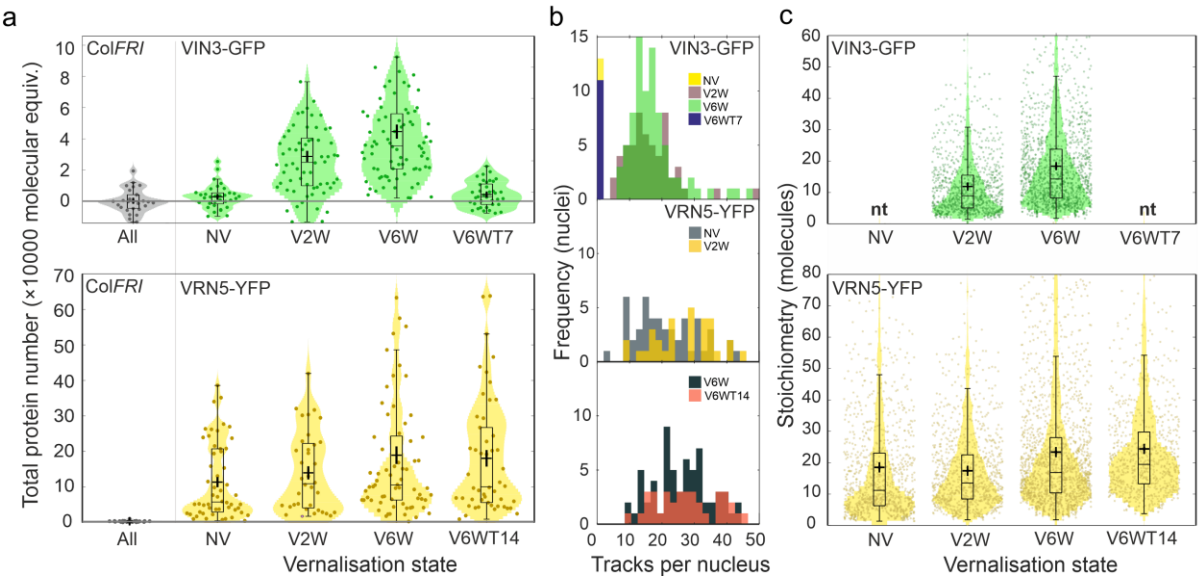

Fig. 4. Cold exposure causes VIN3 and VRN5 to form higher stoichiometry assemblies, but only VRN5 assemblies become more numerous. a) Distributions of integrated nuclear intensity (total number of labelled molecules per nucleus prior to correcting for autofluorescence) of individual nuclei collated from cells imaged at working depths of 20 µm ± 10 µm at different timepoints before, during and after vernalisation, for VIN3-GFP and VRN5-YFP: NV = not vernalised; V2W = two weeks of cold; V6W = six weeks of cold; V6W+T7 = six weeks of cold followed by one week of warm conditions; V6W+T14 = six weeks of cold followed by two weeks of warm. The total protein number is calculated as the excess of the integrated nuclear intensity above the mean level of the autofluorescence background in the negative control line, Col*FRI* (horizontal line). Bar, box and whisker denote median, interquartile range (IQR) and 1.5× IQR respectively; cross: mean ± sem. The abundance of VIN3 protein was insignificant prior to vernalisation (Brunner-Munzel (BM) test vs Col*FRI*, N=66, p=0.11 |ns: not significant at adjusted p<0.01). However, the VIN3 total protein number increases sharply to ~28,000 ± 3,700 molecules above control after 2 weeks cold (N=64, p=0.0031 |*), and peaks at ~44,000 ± 4,700 after 6 weeks cold (N=83, p<0.001 |**). Following transfer to warm conditions, VIN3-GFP levels reduce to ~3,200 ± 1,600 molecules within 7 days (N=74, p=0.04 |ns). VRN5 levels increase between non-vernalised and post-vernalised timepoints from ~110,000 ± 23,000 to ~190,000 ± 37,000 molecules (N=94, p=0.0089|*). b) Distributions of number of tracks per nucleus (binned in columns of width 2 for clarity). The number of VRN5 tracks increases initially (NV: 20.8 ± 1.9 up to 26.8 ± 1.6 tracks per nucleus at 2 weeks cold; N=86, p=0.0054|*) and this increase is retained after 6 weeks' cold (27.0 ± 1.5 and 26.2 ± 2.6 tracks per nucleus at 6 weeks cold and 14 days post-cold respectively; N=94, p=0.80|ns); c) Collated distributions of stoichiometry (number of labelled molecules per nuclear assembly) of individual tracks at different timepoints before, during and after vernalisation; *nt*: no tracks detected.

459 We also explored the effect of transgene copy number on the abundance of VEL proteins
460 during cold exposure. We generated a homozygous single transgene copy line of VIN3-
461 SYFP2, though not in a deletion background, meaning endogenous VIN3 is also present at a
462 similar level (Supplementary Fig. 5a). The expression of exogenous VIN3 still follows the
463 expected pattern (Supplementary Fig. 7) but at much lower levels than in VIN3-GFP,
464 reflecting the reduction to a single transgene copy of *VIN3*. We used SlimVar to estimate
465 the characteristic molecular brightness for SYFP2 to quantify the total protein number in the
466 VIN3-SYFP2 line (Supplementary Fig. 11). Considering only the labelled VIN3 in the SYFP2
467 line, the total protein number is 31 ± 4 % of that of the VIN3-GFP line at both of the two
468 timepoints. Accounting for the unlabelled copy, this rises to 62 ± 11 %. This is consistent
469 with the VIN3-GFP line having three transgene copies, with each copy generating the same
470 amount of protein as the endogenous *VIN3* gene independent of tag.

471 In both VIN3 fusions, the total protein number exhibits an increase from two to six weeks of
472 cold (Fig. 4a and Supplementary Fig. 11a.), although the distributions partially overlap
473 between the timepoints. The two-week level is between half to two-thirds of the six-week
474 level that approaches full vernalisation. For these lines containing 1–3 copies of VIN3, this
475 steady upregulation does not appear to change from that of a single functional copy.

476 We then asked whether these cold-dependent increases in protein abundance are
477 evidenced as higher stoichiometry assemblies, or a greater number of assemblies.
478 Identifying these with stoichiometry and number of tracks detected per nucleus
479 respectively, we saw SlimVar as a uniquely powerful tool to address this question *in vivo*.

480 Highly mobile fluorescent foci for both VIN3 and VRN5 could be tracked for up to ~20
481 consecutive image frames before photobleaching of nuclear contents occurred
482 (Supplementary Videos 1-3). Using bespoke ADEMScode tracking software (Methods) we
483 found that these nucleoplasm-localised protein assemblies were largely excluded from the
484 nucleolus, evident as dark regions 3–6 µm in diameter (Fig. 1k and Supplementary Figure 8).
485 In larger nuclei, the centres of nucleoli also appeared to exhibit weak VIN3 and VRN5
486 localisation (Fig. 3b-c and Supplementary Figure 8). About 1–2% of the total protein number
487 was detected in tracks, which compares well with our estimate, based on the depth-of-field
488 (Supplementary Fig. 2a), that 4–6% of the mean nuclear volume is in sharp focus in each
489 frame.

490 We detected 10–40 tracks per nucleus in the VIN3 line during cold exposure, and for VRN5
491 at all timepoints (Fig. 4b). No tracks were detected either in the Col*FRI* negative control or
492 for VIN3 at pre- or post-vernalised timepoints. A key finding was that the mean number of
493 VRN5 tracks per nucleus increased by ~30% after the onset of vernalisation and this increase
494 was maintained after return to warm (Fig. 4b). We also considered the number density of
495 these tracks (the number of tracks normalised by the nuclear cross-sectional area). The
496 number density of VRN5 tracks similarly increased by about 30% over the vernalisation time
497 course (0.55 ± 0.05 and 0.71 ± 0.05 μm^{-2} before cold and 14 days post-cold respectively:
498 N=62, p=0.0042|*).

499 We found that both VIN3 and VRN5 exhibited broad stoichiometry distributions from a few
500 molecules up to several tens of molecules for individual assemblies (Fig. 4c) and that the
501 average stoichiometry increased with time duration spent in the cold during vernalisation.

502 For VIN3, the mean stoichiometry was 12.0 ± 0.4 molecules at V2W, increasing to 18.6 ± 0.5
503 molecules at V6W (N=1,988, p<0.001|**). For VRN5, assemblies were found to be well
504 developed prior to vernalisation (mean 18.5 ± 0.6 molecules at NV). However, there was an
505 increase in stoichiometry during vernalisation which persisted after the return to warm
506 conditions (mean of 24.4 ± 0.9 molecules at V6W+T14; N=1,626, p<0.001|**). The greatest
507 change occurred during the intermediate stages of vernalisation between V2W and V6W
508 (17.4 ± 0.7 to 23.4 ± 0.6 molecules, N=1,928, p<0.001|**).

509 In summary, the mean number of tracked VRN5 assemblies in each nucleus, and mean
510 stoichiometry of assemblies, each increased over the full course of vernalisation by the
511 same proportion: approximately 30–35%. Thus, the additional VRN5 protein is divided
512 equally into new vernalisation-induced assemblies, as well as into enlarging assemblies that
513 resembled the pre-vernalised state.

514 Conversely, VIN3-GFP increased in total protein number by 58% between two-weeks and
515 six-weeks of cold, which matched the proportional 55% increase in its stoichiometry during
516 the same interval. The number of tracks per nucleus did not increase significantly in either
517 of the VIN3 lines (Fig. 4b and Supplementary Fig. 11). All the additional VIN3 protein
518 generated during vernalisation was incorporated into the existing number of assemblies.

519

520 Multimolecular assemblies of VIN3 and VRN5 contain multiples of two molecules

521 The stoichiometry distributions show a series of periodic peaks (Fig. 5) that are revealed
522 when represented as a kernel density estimate, a method which objectifies the equivalent
523 histogram bin width used.[63] If the assemblies represented have a common oligomeric
524 structure, the characteristic peak-to-peak interval—the periodicity—is equivalent to the
525 number of molecules associated with a physical subunit of the assembly.[64] We developed a
526 new analysis method to discriminate this periodicity using the most common nearest-
527 neighbour peak intervals, verified using realistic statistical simulations and experimental
528 data from standard LacI tetramers *in vivo* [65] (Methods, Supplementary Figs. 9 and 10). Both
529 VIN3 and VRN5 exhibit neighbouring peaks in their stoichiometry distributions separated by
530 two molecules (Fig. 5 insets).

531 We performed SlimVar on the VIN3-SYFP2 line (Supplementary Fig. 11). Our analysis
532 indicated VIN3-SYFP2 has averages of total protein number, stoichiometry and periodicity
533 consistent with the VIN3-GFP line, but only when corrected for the proportion of unlabelled
534 VIN3 present, as estimated from qPCR (Supplementary Fig. 5). We estimated the correction
535 factor by taking the ratio of mRNA expression levels of VIN3 to SYFP2, then normalising by
536 the ratio of VIN3 to GFP expression in the green line, which lacks endogenous VIN3. While
537 inference of quantitative protein levels from mRNA levels is limited, the dependence of the
538 observed periodicity on labelling provides further confidence: if the observed oligomeric
539 species were artifacts mediated by self-interactions of the fluorescent protein tags,[66] the
540 periodicity of visible oligomers would not vary in proportion to unlabelled VIN3. Together,
541 these observations are consistent with VEL proteins dimerising within higher-order
542 oligomeric assemblies *in vivo*. It is intuitive to think of these oligomers growing with the
543 addition of dimeric units, though we cannot test this directly; we do not probe the

544 molecular kinetics or structure that would indicate the pathways of scaffold assembly and
545 disassembly.

546

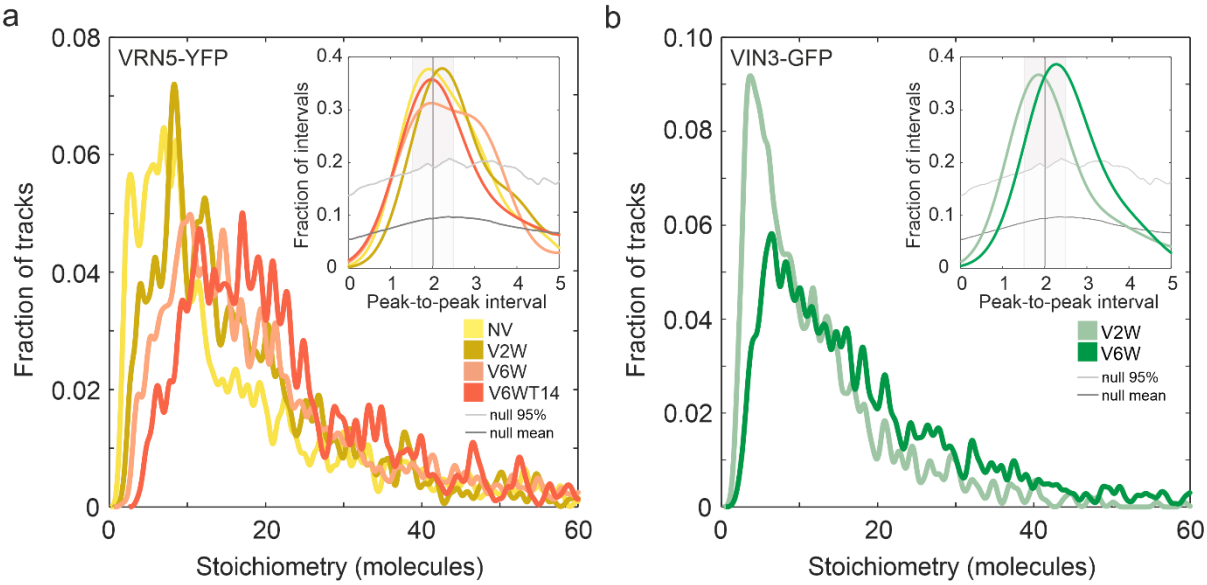

547

548

549 **Fig. 5. VIN3 and VRN5 assemblies exhibit a two-molecule spacing in their stoichiometry**
550 **distributions.** The number of labelled molecules in each assembly (stoichiometry) shows
551 consistent peak-to-peak spacing via periodicity analysis of a) VRN5-YFP and b) VIN3-GFP
552 across different vernalisation timepoints: NV = not vernalised; V2W = two weeks of cold;
553 V6W = six weeks of cold; V6WT14 = six weeks of cold followed by two weeks of warm
554 conditions. A kernel width (curve smoothing parameter) of 0.6 molecules was used
555 corresponding to the standard deviation in the observed intensity of a single molecule at
556 the sifting signal-to-noise threshold. Insets: Periodicity analysis - the number of molecules in
557 this subunit can be estimated from the most common spacing between neighbouring peaks
558 in each stoichiometry distribution. The threshold above which a null (aperiodic) distribution
559 can be rejected is the 95th percentile fraction of intervals (grey trace) output from simulated
560 random stoichiometry (Methods). The most common interval is given by the modal kernel
561 density estimate ± s.e.m. above the null threshold (VIN3-GFP: V2W, 1.9 ± 0.3; V6W, 2.2 ±
562 0.3. VRN5-YFP: NV, 1.9 ± 0.4; V2W, 2.2 ± 0.4; V6W, 2.0 ± 0.3; V6W+T14, 2.0 ± 0.4). The
563 periodic unit in each of these cases is consistent only with an assembly subunit of 2
564 molecules of either VIN3-GFP or VRN5-YFP.

565

566 Mobility of larger VIN3 and VRN5 assemblies matches that of *FLC* during cold
567 exposure

568 We estimated microscopic diffusivity *D* for each detected track by calculating the gradient to
569 the initial portion of its corresponding mean square displacement (Methods).

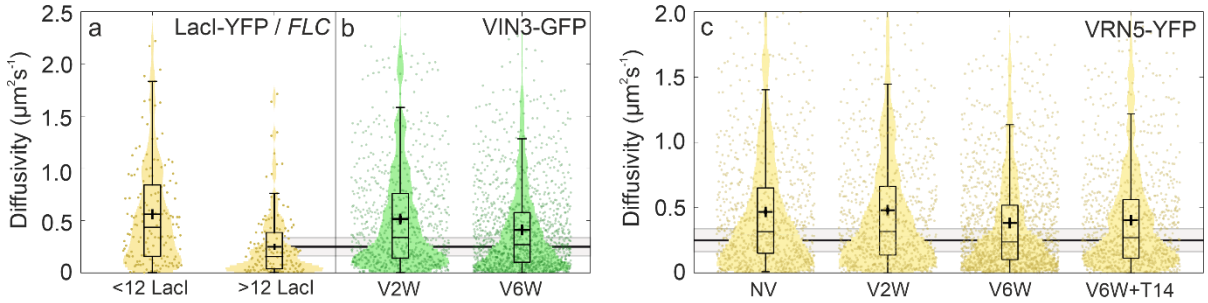

Fig. 6. Microscopic diffusivity of VIN3 and VRN5 assemblies decrease towards that of *FLC* loci during vernalisation. a-d) Diffusivity *D* of individual tracks estimated from mean-square displacement analysis at different vernalisation timepoints: NV = not vernalised; V2W = two weeks of cold; V6W = six weeks of cold; V6WT14 = six weeks of cold followed by two weeks of warm conditions. a) LacI-YFP tracks of fewer than 12 molecules, detected from nuclei without pre-bleaching and identified as unbound LacI, and of LacI-YFP tracks of more than 12 molecules after pre-bleaching, identified as *FLC* candidates; b) Diffusivity of VIN3-GFP and c) VRN5-YFP before, during and after vernalisation. VIN3-GFP and each exhibit a decrease in mobility during the latter part of vernalisation, persisting in VRN5 following return to warm conditions: (VIN3-GFP: D = 0.52 ± 0.03 to 0.41 ± 0.01 $\mu m^2 s^{-1}$; mean ± sem; N=672, p=0.0011|*; VIN3-SYFP2: D = 0.58 ± 0.02 to 0.49 ± 0.02 $\mu m^2 s^{-1}$; N=1,552, p<0.001|**; VRN5-YFP: 0.47 ± 0.02 / 0.48 ± 0.02 $\mu m^2 s^{-1}$ at NV / V2W to 0.38 ± 0.01 / 0.40 ± 0.02 $\mu m^2 s^{-1}$ at V6W / V6W+T14; N≥982, p=0.0072 |*). Horizontal lines denote diffusivity of *FLC-lacO*/LacI-YFP foci under the same conditions (solid line: mean value; grey area, agreement within error).

For comparison with the diffusivity of *FLC* loci, we performed SlimVar imaging of a *FLC-lacO*/LacI-YFP line with 120 *lacO* copies integrated downstream of the *FLC* transgene [67]. To obtain a qualitative indication of the proportion of VIN3 and VRN5 assemblies which might be bound to *FLC* and their stoichiometry, we analysed just tracks whose diffusivity was comparable to that of a typical *FLC* locus (D_{FLC} = 0.20 $\mu m^2 s^{-1}$, Supplementary Fig. 6) within individual track measurement error (± 0.07 $\mu m^2 s^{-1}$) such that D lies in the range 0.13 – 0.27 $\mu m^2 s^{-1}$ (Fig. 6a). This simple method of diffusivity matching [68] is particularly helpful when only single-label lines are available. The subset of VIN3 or VRN5 assemblies with diffusivity consistent with *FLC* (Supplementary Table 1) have stoichiometries distributed similarly to the full cohort of VIN3 or VRN5 tracks (Fig. 5c) and show similar increases in stoichiometry over the course of vernalisation for both VIN3 and VRN5. The median stoichiometry of each protein using this diffusivity matching was in the range 10–20 molecules per assembly, increasing with vernalisation.

We found that VIN3 assemblies became significantly less mobile between two and six weeks of cold exposure (Fig. 6b, Supplementary Fig. 11e). VRN5 assemblies exhibited a similar ~20% decrease in diffusivity during the same central stage of vernalisation (Fig. 6c). In

606 keeping with the increase in stoichiometry and lower diffusivity, the proportion of VIN3
607 assemblies that show slow *FLC*-like diffusion increases from around 11–15% during early
608 stages of vernalisation up to around 17–18% (Supplementary Table 1). The fraction of *FLC*-
609 like VRN5 assemblies present in the nucleus is already ~18% prior to vernalisation and
610 maintains this level throughout. However, given the greater concentration of VEL protein
611 assemblies compared to *FLC* loci, this proportion is unlikely to be representative of VEL
612 localisations at *FLC*, which if present would be a minority observable only by direct
613 colocalisation.
614

615 ## VRN5 assemblies at *FLC* have higher stoichiometry during and after vernalisation

616 To directly track VRN5 at the *FLC* locus, we generated transgenic plants co-expressing VRN5
617 (fused to mScarlet-I [69], mScI) and *FLC-lacO* (via LacI-YFP) for dual-colour SlimVar. Our test for
618 colocalisation of VRN5 at *FLC* first required a reliable method to identify *FLC* without
619 perturbing the mScarlet-I reporter for VRN5. For each nucleus, we first performed a rapid z-
620 stack using 514 nm wavelength laser excitation to screen for and localise bright, low
621 mobility LacI-YFP foci consistent with *FLC* genomic loci (Fig. 7a). At a chosen z-position
622 containing one or more of these *FLC* candidates, we then tracked VRN5-mScI and LacI-YFP
623 using alternating laser excitation (Methods); most images were dominated by the presence
624 of unbound LacI-YFP foci, however, we measured a distinct subset bound to *FLC* (Fig. 7b)
625 with a frequency of 2.3 ± 1.4 (mean ± s.d.) per nucleus in the meristem, matching the
626 expectation of 2 *FLC* loci per nucleus within experimental error [67]. This rose to 3.3 ± 1.7 in
627 cells toward the transition zone, consistent with more nuclei exhibiting additional pairs of
628 *FLC* loci under genomic endoreduplication. Approximately 40% of detected *FLC* loci were
629 colocalised with VRN5-mScI assemblies, though this proportion was constant across all
630 vernalisation times. This led us to question: might a putative memory element be
631 conditional on the properties of the colocalised VRN5 assemblies, such as stoichiometry?
632

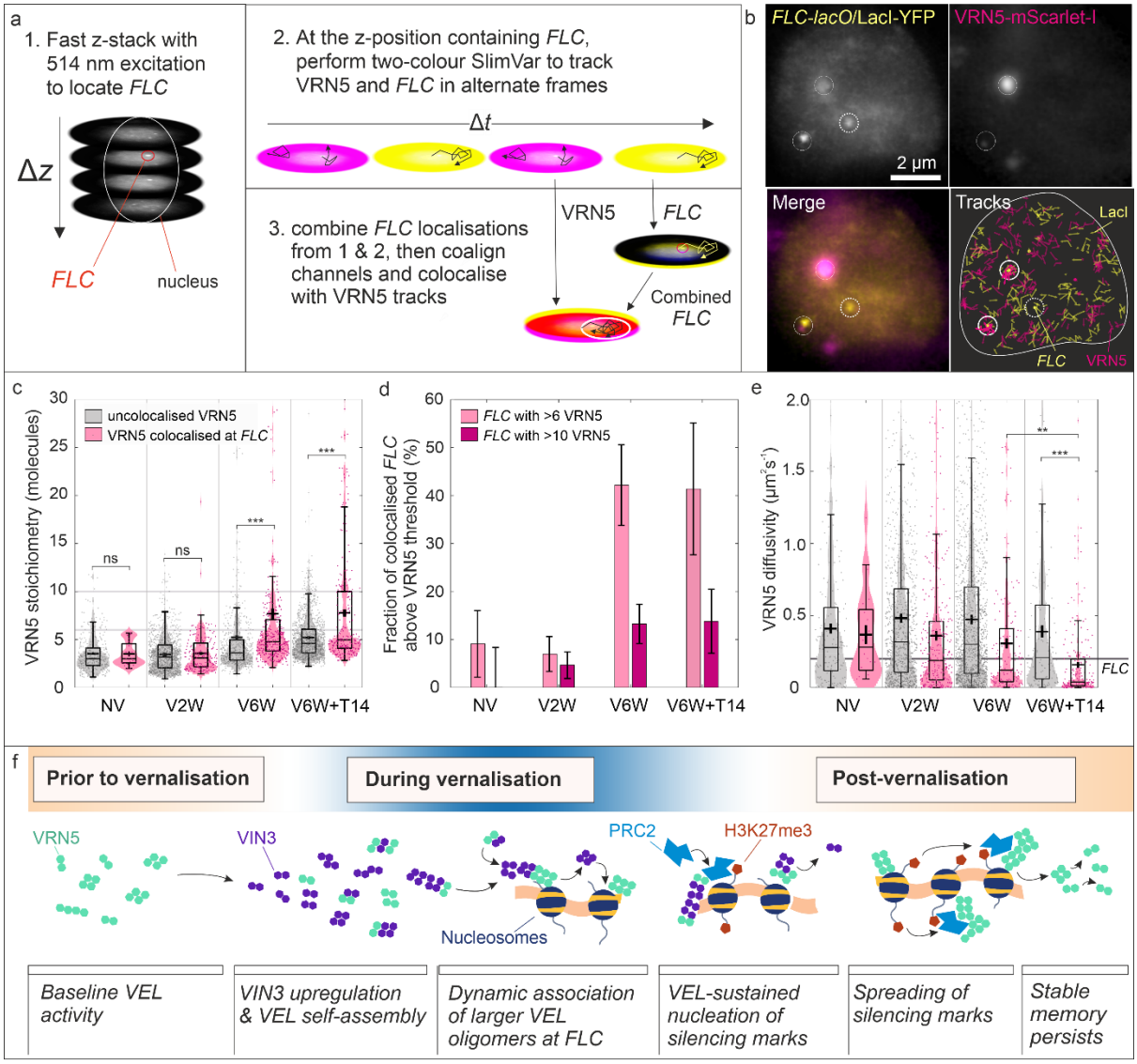

Fig. 7. A dynamic subset of enlarged VRN5 assemblies is present at *FLC* loci after long cold exposure and after return to warm.

a) Representative example of a z-stack used to screen for *FLC* loci in the LacI-YFP channel, followed by b) two-colour alternating excitation at a single target z-plane to capture *FLC* loci (circles) and colocalisation events (solid circles) between *FLC* (yellow) and VRN5-mScI assemblies (magenta) as determined by tracking (Methods). The example shown is at six weeks of cold exposure. Note that the genomic loci *FLC-lacO*, rather than individual nucleosomes, are localised experimentally by LacI-YFP in yellow tracks. c) The mean stoichiometry of VRN5 colocalised at *FLC* exceeds that of uncolocalised VRN5 because of vernalisation. The timepoints are: NV = not vernalised; V2W = two weeks of cold; V6W = six weeks of cold; V6W+T14 = six weeks of cold followed by two weeks of warm conditions. The difference is initially negligible before vernalisation (3.5 ± 0.3 vs 3.5 ± 0.1, NS, p=0.39, N=365) but appears clearly at V6W (7.7 ± 0.6 vs 5.0 ± 0.2, p<0.0001***, N=2867) and is sustained for at least two weeks after return to warm (7.8 ± 0.5 vs 5.2 ± 0.2, p<0.0001***, N=1416). d) Vernalisation increases the fraction of colocalised *FLC* with VRN5 above a

651 stoichiometry threshold. Total number of detected *FLC* (Supplementary Table 2) found to be
652 colocalised with VRN5 are: (NV) 11, (V2W) 43, (V6W) 83, (V6W+T14) 29. Thresholds are set
653 at which dependence on vernalisation becomes statistically significant (>10 molecules) or
654 maximal (>6 molecules). The proportion of colocalised *FLC* associated with >6 VRN5
655 molecules are (NV) 1/11 and (V2W) 3/43, while this frequency rises with vernalisation to
656 (V6W) 35/83 and (V6W+T14) 12/29 colocalised *FLC.* The increases between two and six
657 weeks, and between two weeks and return to warm are significant (Fisher's exact test two-
658 tailed, $p=7 \times 10^{-4}$ and $p=3 \times 10^{-5}$ respectively). e) The diffusivity of VRN5-mScI tracks either
659 colocalised to *FLC* (decreasing with vernalisation) or independent of *FLC.* f) An illustration of
660 the model supported by the imaging results. The model uses *FLC* as the locus, showing VEL
661 protein dynamic self-assembly and function in vernalization-driven epigenetic silencing;
662 prior to vernalisation, VEL proteins interact with each other and PRC2, but the assemblies
663 are modest in size and the majority diffuse too quickly to be dependent on interaction with
664 chromatin. During vernalisation, the VEL assemblies become larger and preferentially
665 localize at *FLC* compared to their status prior to vernalization, consistent with facilitating
666 greater PRC2-mediated nucleation of silencing marks. Large VRN5 assemblies persist at *FLC*
667 after the cold stimulus is removed, which may assist the sustained spreading of marks and
668 maintenance of vernalisation memory.

669

670 Both number and stoichiometry of VRN5 assemblies were considerably lower in this single-
671 copy VRN5-mScI line than the multiple-copy VRN5-YFP line (Fig. 4c). Like VRN5-YFP,
672 however, these VRN5 assemblies showed stoichiometries that increased with vernalisation
673 independent of colocalisation at *FLC* (Fig. 7c, grey). There was a proportionally far greater
674 increase in stoichiometry of VRN5 assemblies colocalised at *FLC,* particularly after long cold
675 exposure and after the return to warm (Fig. 7c, magenta). Correspondingly, the fraction of
676 colocalised *FLC* sites associated with assemblies of more than 6 VRN5 molecules increased
677 around fourfold to approximately 40% between two and six weeks of cold (Fig. 7d). At six
678 weeks' cold, the frequency of *FLC* loci colocalised with >6 VRN5 molecules exceeded an
679 average of one site per nucleus. This preferential colocalisation of FLC with larger VRN5
680 assemblies after six weeks of cold and on return to warm was detectable for thresholds
681 between 5–10 VRN5 molecules.

682 To establish the timescale of interaction between VRN5 and *FLC*, we then compared their
683 mobility (Fig. 7e). Before cold and at two weeks of cold exposure, the mean diffusivity of
684 the colocalised VRN5 assemblies exceeded that of *FLC* loci by a factor of ~3, indicating short-
685 lived binding relative to the ~10 ms sampling timescale. After six weeks of cold and after
686 return to warm, the diffusivity of colocalised VRN5 ever more closely matched the typical
687 diffusivity of *FLC* loci, potentially pointing to a tighter interaction. Notably, the fraction of
688 VRN5 not colocalised at *FLC* remained at the higher diffusivity independent of vernalisation.
689 An unexpected observation was the rapid rate of VRN5 turnover at *FLC* that is sensitive to
690 assembly size. The mean apparent residence time [70] at *FLC* of colocalising assemblies
691 smaller than 6 VRN5 was 26 ms before, and 34 ms after, vernalisation, distinctly shorter
692 than the typical photobleaching time of 63 ± 2 ms. For assemblies larger than 6 VRN5 after
693 vernalisation, the residence time was 64 ± 6 ms, indicating minimal dissociative loss on this

694 timescale relative to photobleaching. This difference indicates turnover of smaller
695 assemblies at *FLC* on subsecond timescales, in contrast to less transient binding of larger
696 assemblies.
697
698 In Lövkvist et al., 2021 [17], an assembly size of 17 was predicted as the best fit to
699 observations of nucleating silencing marks, potentially reducing further to 10 in the case of
700 maximal positive cooperativity. Although we do not know whether VIN3 assemblies
701 colocalise specifically with *FLC*, and if so, the size of such an assembly, a large minority of
702 observed VIN3 and VRN5 assemblies with sufficiently low mobility to interact with *FLC*
703 clearly do exceed this size threshold during and after vernalisation. In the case of VRN5, we
704 show this is exceeded by a small minority of assemblies directly colocalised with *FLC* only
705 after vernalisation, though at a single gene copy, the maximal distinction with uncolocalised
706 assemblies occurs at even lower thresholds of as low as 6–10 molecules. This finding
707 suggests that if any lower bound size is required for positive feedback to become active in
708 these colocalised assemblies, it must be very low.
709

710 Discussion

711 Here, we have developed a new optical microscopy pipeline—SlimVar—and applied it to
712 image cell nuclei in *Arabidopsis* root tips. SlimVar is optimised to detect single fluorescent
713 protein fusions by sampling faster than their typical motion in cells. It therefore enables
714 tracking of molecular assemblies diffusing in comparatively deep, multicellular samples,
715 without requiring complex protocols for chemically conjugating target biomolecules.
716 In animal tissues, studies using HILO [61 71], lightsheet [72 73] or lattice lightsheet [35] have
717 previously demonstrated single-molecule tracking to a standard of 50 ms sampling at ~300
718 µm depth, or 10 ms at ~30 µm depth using dyes, which is comparable to SlimVar with
719 fluorescent proteins. However, in plant tissues, single particle tracking at molecular
720 sensitivity has been demonstrated with TIRF [74,75], or VAEM [31,33,76–78] only in the vicinity of a
721 surface cell layer. SlimVar therefore advances the ability to track and count single-molecular
722 assemblies in plants, and potentially in a range of tissues, to that of more complex existing
723 microscopy technologies.
724 In achieving this speed, SlimVar trades off some of its 3D capability; the detection of foci is
725 restricted to a limited depth of field much smaller than the nucleus. Nonetheless, it is
726 capable of z-stacks as used here for systematic *FLC* detection, and it should be possible to
727 extend oblique angle [51] or lightsheet-based approaches to achieve rapid volumetric scans [79]
728 and extended depth of field [80]. Within the depth of field itself, astigmatic 3D imaging has
729 been demonstrated with Slimfield [81]. The implementation of better index-matching and
730 photon-efficient adaptive optics [36,82] could also improve the range of accessible working
731 depths currently limited by scattering losses, while also mitigating the required adjustments
732 at each depth. Single-molecule experimental schemes related to SlimVar such as multiple-
733 colour or photoconvertible labelling on the same target [83], may provide promising future
734 avenues to probe the turnover dynamics over longitudinal experiments.

735 As presented here, SlimVar is implemented on a custom microscope with free-space
736 components. However, the optical components and controls are essentially similar to
737 commercial widefield/TIRF microscopes used for single-molecule localisation microscopy.
738 Commercial instruments do not typically provide the intense excitation or detector
739 sensitivity sufficient to track single fluorescent proteins at depth (Supplementary Fig. 2). As
740 such, we use the new platform to explore newly accessible biological insight. In future
741 work, we aim to democratise and enhance SlimVar accessibility further by minimally
742 adapting a representative, modern commercial microscope that meets these requirements.
743 Although optimised for applications in *Arabidopsis* root tips, SlimVar is expected to be
744 adaptable for functional bioimaging research at the molecular scale inside a range of living
745 tissues.

746 Using SlimVar, we demonstrated oligomeric assemblies of the PRC2 accessory proteins VIN3
747 and VRN5. VIN3 and VRN5 assemblies increase in stoichiometry above a demonstrable
748 threshold during prolonged cold. Both sets of assemblies exhibit mobility signatures similar
749 to *FLC* gene loci, with a subset of larger VRN5 assemblies clearly demonstrating *FLC*
750 colocalisation. The higher stoichiometry assemblies are therefore prime candidates to
751 contribute to memory element function predicted in a hybrid model coupling protein self-
752 assembly and histone modification [17]. A major advantage of SlimVar over ensemble
753 techniques is that it directly probes not only whether proteins become abundant (total
754 protein number), but whether such change take effect as higher/lower assembly
755 concentration (tracks per nucleus) or as larger/smaller assemblies (stoichiometry). Our
756 observation that adding more protein subunits preferentially results in a larger average
757 assembly stoichiometry, rather than a greater number of assemblies, is itself consistent with
758 a model of positive cooperativity. Taken together, these findings support the view that VIN3
759 and VRN5 assemblies mediate epigenetic memory over the extended vernalisation cycle of
760 several weeks (Fig. 7f). However, our current imaging results do not make a direct claim
761 about nucleosomes, only about the *FLC* locus reporter, for which the endogenous locus
762 contains at least three nucleosomes in the nucleation region relevant to VEL function.

763 The model [17] makes no predictions as to the underpinning factors and mechanisms - neither
764 for protein self-assembly, nor dynamic exchange with the surrounding nucleoplasm. The
765 head-to-tail polymerization via the VEL domain [23] is likely involved, but the predominantly
766 transient interactions between most individual VEL protein assemblies and *FLC* may suggest
767 that the physical feedback processes are more complex than currently understood. Our
768 current interpretation is that the VRN5 assemblies enriched at *FLC*, of sufficient size to
769 satisfy the model, are most likely simple oligomers. Yet, we contemplate whether the very
770 largest of these (~100 VRN5) are instead small, dynamic, phase-separated condensates,
771 related to those observed during transient overexpression of VEL proteins [19,23,84]. If so, the
772 collective, multivalent interactions characteristic of condensates might offer a longer, or
773 otherwise more effective, residence time at *FLC* than we observed for typical molecular
774 assemblies, and therefore a disproportionate contribution to epigenetic memory. SlimVar is
775 an excellent tool capable and primed to further investigate these rare mechanistic events *in*
776 *vivo*. Further work will investigate the phenotypic and molecular interactions between VRN5
777 and VIN3 mutants [84].

While pioneered for the *Arabidopsis FLC* system, these protein-mediated feedback processes may underpin Polycomb-based epigenetic memory common to all eukaryotic systems. Our study demonstrates the interdisciplinary value at the interface of the physical and life sciences of developing SlimVar, and other bioimaging technologies at single molecule precision, to tackle outstanding biological questions in epigenetic processing and memory.

Methods

Plant material and growth conditions

VIN3-GFP and VRN5-YFP lines have previously been described [11,19]. To generate the VIN3-SYFP2 line, GFP of the pENTR pVIN3::VIN3-GFP construct [85] was replaced by SYFP2 by seamless mega-primer cloning. VIN3-SYFP2 was cloned to the SLJ destination vector, a derivative of SLJ755I5 [86] and transformed to *Agrobacterium tumefaciens* C58 by triparental mating. The transgenic VIN3-SYFP2 plant in Col*FRI* background was generated by floral dipping with *Agrobacterium*. To generate pENTR pVRN5::VRN5-mScarlet-I, the SYFP2 of VRN5-SYFP2 [84] was replaced by mScarlet-I by seamless mega-primer cloning. The VRN5-mScarlet-I was cloned to the SLJ destination vector, a derivative of SLJ6991 [86], transformed to *Agrobacterium tumefaciens* C58 and subsequently transferred into *vrn5-8 FRI* mutants as described above. All primers used are listed in Supplementary Table 3. Transgene copy number was determined in T1 or T2 transformants by IDna Genetics (Norwich Research Park). To generate the plant co-expressing VRN5-mScarlet-I and *FLC-lacO*/LacI-YFP, the VRN5-mScarlet-I line was crossed into the *FLC-lacO*/*lacI-YFP* line [67] and was selected by antibiotics.

All seeds were surface-sterilised and sown on 100 mm growth plates containing Murashige and Skoog (MS) medium (Duchefa) with 1 wt. % agar (Difco Bacto) without sucrose. The plates were sealed with Micropore tape (3M) and kept at 4°C in the dark for 2–3 days to stratify the seeds. Plates were racked vertically in the growth chamber in warm conditions (16 h light/ 8 h dark with constant 22 ± 2°C, 60 ± 10% Relative Humidity (RH)) for 7 days. Non-vernalised timepoints (NV) were then imaged on the final day. For all other timepoints, plants were grown in warm conditions for 7 days as above and then were transferred to cold conditions (8h light / 16h dark, 5 ± 1°C, 50 ± 30 % RH) to vernalise for either 2 or 6 weeks (V2W and V6W respectively). Following vernalisation, a subset of plates was returned to warm conditions for an additional period of either 7 or 14 days (V6W+T7 or V6W+T14). Plates for warm timepoints (NV, V6W+T7, V6W+T14) were handled at room temperature, while those imaged at cold timepoints (V2W and V6W) were transferred on ice to a 4°C cold room for slide preparation to avoid temperature spikes affecting the fragile vernalised state. VIN3 expression is known to be modulated by the cellular circadian clock [10]; to isolate the long-term trends in expression relating to cold exposure, imaging was performed in daylight hours 4–8 to align with the diurnal maximum in VIN3 expression. At least 3 independent vernalisation courses were grown for each line and timepoint (Supplementary Table 2). Immediately prior to imaging the *FLC-lacO*/LacI-YFP lines (single colour or dually labelled with VRN5-mScarlet-I), LacI-YFP was induced by placing opened

820 growth plates next to a bath of 0.5% EtOH at 25°C in an airtight container for 2.5 h. This
821 resulted in an optimal amount of LacI-YFP expression in the meristem for SlimVar imaging
822 without spot-bleaching, below the near-saturated induction level (1.5–2% EtOH for 1.5 h [67])
823 used for confocal study (Supplementary Fig. 9a-d).

824 ## RNA expression analysis

825 Total RNA was extracted using the phenol method as previously described [11,87]. Genomic
826 DNA was removed from the TURBO DNA-free kit (Invitrogen, AM1907) before reverse
827 transcription with SuperScript IV reverse transcriptase (Invitrogen, 18090050) and gene-
828 specific primers. Quantitative PCR analysis was performed on a LightCycler480 II (Roche).
829 Target gene expression was normalised by PP2A (AT1G13320) and UBC (AT5G25760). All
830 primers used in this study are listed in Supplementary Table 3.

831 ## Preparation of samples for imaging

832 Identical slides were prepared for confocal, Airyscan or SlimVar imaging [61]. Briefly,
833 GeneFrames (Thermo Scientific, AB0578) were fixed to standard slides (VWR) and filled with
834 MS medium plus 1 wt.% agarose to produce agar pads. Where necessary due to seedling
835 size, the terminal >10mm of the primary root of each plant was excised using a razor. Root
836 tips were laid on each agar pad with tweezers. Liquid MS media was applied to exclude air
837 and each slide was sealed with a plasma-cleaned #1.5 coverslip (VWR). Each slide was
838 imaged within <1 h.

839 ## Confocal and Airyscan imaging

840 Confocal imaging was performed on a Zeiss LSM880 microscope equipped with argon ion
841 laser and Plan-Apochromat 63×/1.40 NA oil objective lens (Zeiss). Samples were illuminated
842 at 488 or 514 nm wavelengths (GFP or YFP/SYFP2 channels) respectively, and the emission
843 detected at 490–550 nm or 518–550 nm respectively [61]. The root tip confocal images (Fig.
844 3b, Supplementary Fig. 7, Supplementary Fig. 9a-d) were acquired as z-stacks over ≤3 z-
845 slices of 1,000 × 1,000 pixels at 0.6× zoom factor, at 1.5 µm intervals using 20 mW excitation
846 power. Slices were postprocessed in FIJI/ImageJ [88] with a 2D median filter (0.2 µm filter
847 size) to suppress noise before performing a mean z-projection.

848 Timelapse z-stacks of nuclei (Fig. 3c) were acquired in Airyscan RS mode, after aligning the
849 detector with immobilised TetraSpeck microspheres (Invitrogen, 0.1 µm diameter). Each
850 sequence contained ≤25 volumetric cycles, each taking 0.84 s (12 slices × 56 ms/slice). The
851 axial step size was 0.65 µm with 112 × 112 pixels at 14× zoom factor and 20 mW excitation
852 power. The 3D z-stacks were Airyscan post-processed in Zen Black software (Zeiss) with a
853 user-optimised strength parameter of 5.0. Vernalised timepoints at two and six weeks of
854 cold (V2W, V6W) were imaged at 5 ± 1 °C on a water-recirculating Peltier-cooled stage
855 (Linkam PE100) calibrated using hydrocarbon melting points.

856 ## SlimVar imaging platform

857 SlimVar was adapted from a Slimfield microscope comprising objective-lens-based total
858 internal reflection fluorescence (OpenFrame, Cairn Research), custom-built from benchtop
859 optical components (Thorlabs) and a nanopositioning stage (Mad City Labs). A general
860 scheme of Slimfield microscopy is available [43,44,89 48] with key terms defined in Table 1.

861

Metric / Object	Definition
Foci	Spot-like local intensity maxima in a single frame, each corresponding to a localised group of labelled molecules. Associated properties include spatial/temporal location, total intensity, and signal-to-noise ratio.
Track	A set of foci in adjacent frames which are spatially close enough to form a contiguous trajectory. Associated properties include those of the set of foci, plus stoichiometry, diffusivity, and signal-to-noise ratio.
Characteristic molecular brightness	The average number of photon counts per frame associated with a single fluorescent reporter molecule (e.g. GFP), under a fixed imaging condition. Equivalent to the number of photons in the most common intensity step observed for tracks in the final stage of photobleaching.
Integrated nuclear intensity	The total fluorescence intensity, including autofluorescence, of an entire nuclear segment in photon counts, normalised by the characteristic molecular brightness. Dimensionless; described in fluorescent protein equivalents.
Total protein number	The average number of labelled molecules in a nucleus, not including autofluorescence, estimated from the difference in integrated nuclear intensity from that of an unlabelled negative control.
Stoichiometry	The number of labelled molecules in a track, as estimated by dividing the track's initial intensity by the characteristic single-molecule brightness.
Periodicity	The number of labelled molecules in a repeat unit within tracked objects, as estimated by the consistent stoichiometry intervals between nearest-neighbour peaks in the stoichiometry distribution.
Diffusivity	An average measure of the rate of random microscopic motion of a track based on the increase in its mean-squared displacement over time.
Signal-to-noise ratio (SNR)	A measure of the signal strength of foci or tracks compared to background noise. Higher SNR implies higher confidence of a true positive detection.
Sifting	Sifting is the postprocessing step which imposes a minimum SNR threshold on foci and tracks, and a minimum track length, to improve robustness of the track-wise metrics.

Table 1. Glossary definitions of analysis metrics for single particle tracking.

With increasing acquisition depth, refractive index mismatch between immersion oil and aqueous sample is a key challenge [56] due to spherical aberration and excitation beam deviations. This is usually avoided with expensive water or silicone immersion objective lenses, but we demonstrate equal or superior performance with an affordable oil immersion objective lens: NA 1.49 Apo TIRF 100× oil (Nikon). For Slimfield and SlimVar, as with other single-molecule techniques with widefield detection, objective lenses must have a large back aperture diameter, common in lenses specialised for TIRF. Single molecule sensitivity was afforded by a fast sCMOS camera (Teledyne Photometrics Prime95B, 12-bit 'Sensitivity', or BSI, 16-bit 'Sensitivity' i.e. gain of 0.6 photoelectrons per count with an offset of 100 counts). The turret dichroic mirror was either dual-band for GFP/mScarlet-I (Chroma ZT488/561rpc) or for YFP/mScarlet-I (Chroma ZT442/514/561rpc) as appropriate. A 580 nm wavelength longpass beamsplitter (OptoSplit, Cairn Research) after the tube lens (f=200 mm achromat, ThorLabs AC254-200-A-ML) enabled simultaneous detection of GFP (525/50 nm wavelength centre/bandwidth emission filter) or YFP (550/25 nm) in a green/yellow channel, and mScarlet-I (594/25 nm) in a red channel. Additional magnification (1.2 – 2.2×) was used to compensate for different camera pixel sizes to maintain an oversampled pixel width of 53 ± 5 nm in the images.

Continuous wave lasers (Coherent OBIS) delivered Gaussian beams (TEM_{00}) at 488 nm, 514 nm and 561 nm wavelengths with 1.9 mm FWHM beam diameter that were circularised by an achromatic quarter waveplate [90]. These were steered and focused at the objective back aperture using f=150 mm lenses to collimate them through the sample with a FWHM diameter of 25 µm.

To optimise background contrast for *Arabidopsis* root tips, the following adaptations were made to the Slimfield microscope:

i) the second convex lens in the expansion telescope was mounted on a lateral translation stage with a high-precision micrometer; this shift (up to 2.3 mm) generated an equivalent lateral displacement of the beam at the 6 mm diameter objective back aperture, thereby tilting the beam away from the optic axis at the sample. The beam delivery angle was calibrated for lens micrometer position following [49] and set to 50° ± 3° from normal incidence in oil, corresponding to 60° ± 5° in water by Snell's Law, with minimal coupling into the evanescent field at the coverslip, similar to HILO [51] but unlike PaTCH [91] or VAEM [50–52,92].

ii) a field stop was placed in the conjugate plane upstream of the first telescope lens. Rather than thinning the beam with rectangular slits to further suppress background,[52] we chose to maintain a circular beam; this illuminated the full depth of each nucleus for representative estimates of nuclear protein copy and efficient screening of *FLC* loci. The stop was tightened to crop the beam from 25 µm FWHM to between 4–9 µm cross-section. The field then approximated an ellipse of $1 \times 3^{1/2}$ the chosen beam cross-section, or 4–16 µm diameter, uniformly illuminated at a power density of 1–5 kW cm^{-2}, which is a few-fold less than the saturation excitation intensity of the fluorescent proteins.[58]

iii) a pair of mirrors were used to incline the beam ~5 mrad away from the optic axis at its intersection with the objective back aperture. This compensates the beam's mismatch-dependent lateral deflection of ~11 µm at the 25 µm calibration depth.

908 The aberrations were then corrected using the following protocol.

909 ## Optical calibration protocols

910 Two forms of calibration are presented: basic, relying only on high-signal fluorescence with
911 a correction collar, or an advanced protocol, also using single molecules and tube lens shift.
912 For best results, the advanced protocol requires independent z-positioning of the objective
913 lens and the sample stage, since this enables decoupled correction of both defocus and
914 spherical aberrations.

915 **Basic aberration correction with objective collar only**

916 1. Choose a nominal working depth (e.g. d = 25 µm).
917 2. Prepare a sample with sub-diffractive fluorescent features at this desired working
918 depth or deeper. This could comprise a suspension of fluorescent beads of diameter
919 <200 nm (Fluospheres, Invitrogen) in 1 wt.% agarose, or weakly autofluorescent
920 point-like features in a root tip.
921 3. Set the laser excitation to a modest level to reduce photobleaching, e.g. 0.2 mW
922 source power ~ 0.1 kW/cm^2 irradiance and a long exposure time ~100 ms.
923 4. Move the stage (or objective lens) to focus on the upper surface of the coverslip,
924 then move an additional distance corresponding to the nominal working depth.
925 5. Move the stage laterally to find a point-like sample feature close to best focus.
926 Centre it in the field of view without refocusing.
927 6. Acquire a z-stack at <0.2 µm spacing over a maximum range of ± 2 µm.
928 7. Repeat steps 4–6 for several such features.
929 8. Repeat steps 4–5 to find a new feature. Find best focus using the objective.
930 Iteratively decrease the collar setting to a thinner coverslip setting
931 (by $n_{water}/n_{oil} \times d$ = 30 µm, i.e. to ~140 µm) and refocus the objective to achieve best
932 lateral focus (narrowest width of the feature).
933 9. Repeat steps 4–7 but with the new collar setting, to generate a second set of z-
934 stacks. Compare the differences in PSF (e.g. using MetroloJ QC).

935 **Advanced aberration correction with single molecule sample and tube lens shift**

936 1. First, mark the tube lens position. It is best to set any components such as filters
937 between the objective lens and the detector, before—rather than after—performing
938 the calibration.
939 2. Measure the total image magnification using a graticule.
940 3. Choose a nominal working depth (e.g. d = 25 µm). Prepare samples containing sub-
941 diffractive fluorescent features and slow (or immobilised) single molecules at this
942 desired working depth, such as a dilute (<1 nM) suspension of fluorescent proteins
943 and/or beads in 1 wt.% agarose, or on a tilted coverslip (Supplementary Fig. 2a).
944 4. Set the laser excitation to a high level, e.g 10 mW power or ~5 kW/cm^2 irradiance
945 with 10 ms exposure time. Adjust the camera to the corresponding imaging settings
946 above for the 'balanced mode'.
947 5. Focus on the coverslip and move to the nominal working depth using the sample
948 stage only (e.g. d = 25 µm)

6. Move the stage to a point-like sample feature near focus (this could be a single bead or a section of the volume or surface containing single molecules in focus). Centre it in the field of view.
7. Acquire several fields of view for reference: for beads, acquire z-stacks with <0.2 µm spacing over a range ± 2 µm. For fields of view containing visible single molecules, acquire multiple SlimVar sequences with >300 frames; a longer exposure time may be needed to distinguish single-molecule foci from background. Note this exposure time.
8. Iteratively decrease the collar setting to a thinner coverslip setting (by $n_{water}/n_{oil} \times d$ = 30 µm, i.e. to ~140 µm) and move the stage (not the objective lens if possible) to achieve best lateral focus corresponding to the narrowest width of the feature.
9. Move the objective lens towards the sample (or if this is not possible, move the sample stage towards the objective) a further 20% of the working depth (e.g. by 4 µm to a new total working depth of 29 µm).
10. Compensate by moving the tube lens towards the objective (by up to 40 mm for a 200 mm focal length lens) until the plane of best focus is pulled back onto the chosen feature.
11. Using the stage, re-centre the feature in the field of view. If the region has bleached, pan the stage sideways to a new feature or field of view at the same depth.
12. Then, adjust the collar setting for best lateral resolution as above. Refocus onto the feature (preferably using the objective lens).
13. Repeat the acquisitions in the calibrated state: starting from 10 ms, adjust the exposure time until single molecules are visible. Acquire multiple fields of view in SlimVar sequences containing visible single molecules and track in ADEMScode. Compare the SNR of single molecules. If the exposure time was longer for the reference set, divide the reference SNRs by the square root of the ratio of exposure times. For beads, acquire z-stacks with <0.2 µm spacing. Compare the differences in axial and lateral resolution from the reference state (e.g. using MetroloJ QC).
14. Further iteration of focal position with either collar setting or tube lens position may be desirable for best results, as determined by minimal axial FWHM and maximum signal-to-noise metric.
15. Finally, measure the total image magnification using a graticule, as this may have changed from the nominal design magnification.

Evaluation of the advanced calibration

We implemented the latter protocol using a combination of *in vitro* YFP (Supplementary Fig. 2) and fluorescent beads (Supplementary Fig. 3). This introduced a correction collar setting of 140 µm (for a coverslip #1.5H of 170 µm thickness) and a shift of d = -32 mm in an f = 200 mm tube focal length (Supplementary Fig. 3). Despite this shift in the tube lens position, we found the optical pixel size remained consistent within the range 53 ± 5 nm, implying a change in magnification no larger than -8%. This is less than the drop of d/f ~ -16% expected from a formal change in tube length, i.e. using a tube lens with a different focal

992 length of ($f + d$) to restore the 4f imaging condition. Since the imaging is improved, the sine
993 condition between the sample and the intermediate image planes must be maintained,
994 which suggests that infinite conjugation breaks down: the emission reaching the camera is
995 no longer parallel to the optical axis at the back aperture of the objective. This also explains
996 the observed reduction in effective numerical aperture by a factor of approximately $(1 -$
997 $d/f)^{1/2}$ ~ 8% from 1.49 to ~1.38 (Supplementary Fig. 2). We suppose that relaxing the infinite
998 conjugation enables the combined calibration elements to deliver not only the required
999 amount of spherical aberration, but also the correct amount of wavefront defocus[55] for
1000 deeper imaging. This result suggests this strategy is workable for small defocus
1001 compensations, without introducing a different tube lens or using e.g. spatial light
1002 modulators that can provide separable, tuneable corrections to defocus and spherical
1003 aberration. However, the beamsplitters and other elements between the objective and
1004 tube lens would ideally need to be kept constant between calibrations.

1005 The calibration yields a minimal FWHM of detected foci ~170 nm (Fig. 3d) and a localisation
1006 precision[93] of 40–80 nm (Supplementary Fig. 12). In plants we see a net increase of 2.6 in
1007 the median signal-to-noise ratio relative to epifluorescence microscopy, when accounting
1008 for the decreased exposure time (normalised by the square root of exposure time ×
1009 excitation power, n = 500 foci, Supplementary Fig. 2j).

1010 Settings for SlimVar imaging in plants

1011 Nuclei were identified in brightfield to find best focus at the nucleolar midbody without
1012 photobleaching and were captured for manual segmentation. Fluorescence acquisition
1013 settings in green, yellow and/or red channels were pre-optimised to avoid initial camera
1014 saturation and to ensure detection of individual tracks of molecular brightness for GFP,
1015 SYFP2 / YFP, and mScarlet-I respectively. Three exposure times were used: i) a
1016 'representative' 20 ms providing a low-bias detection of all particles down to single
1017 molecules, ii) 'fast' 2 ms to ensure robustness of tracking fidelity and mobility
1018 measurements of only the brightest assemblies, and iii) a 'balanced' 10 ms, also capable of
1019 single molecule detection. Fast acquisitions captured the subset of assemblies with fourfold
1020 (upper quartile) mean stoichiometry at a tripled detection rate due to the faster sampling
1021 bandwidth. Results shown derive from data collected with the representative (VRN5-YFP
1022 and VIN3-GFP lines) or balanced mode (VIN3-SYFP2, *FLC-lacO*/LacI-YFP and VRN5-mScarlet-I
1023 lines) unless otherwise stated. These settings were fixed to minimise systematic variation in
1024 the characteristic molecular brightness (Supplementary Fig. 1).

1025 The region of interest spanned ≤300 rows (16 µm) giving a readout time of 2.7 ms per
1026 frame, and sampling rates of 44–217 fps. Lasers were triggered in each frame by the
1027 camera in 'All Rows' mode to provide global shuttering without extraneous photobleaching.
1028 To capture photoblinking, the number of frames in each sequence was set to >50× the
1029 photobleaching decay constant.

1030 Protein tracking, sifting and intensity analysis

1031 SlimVar analysis used batches of OME TIFF image sequences as input to MATLAB-based
1032 ADEMScode v2.2 software [94,45], whose key features are also available in open-source Python
1033 package PySTACHIO [95]. The fluorescence sequences were cropped to specify individual

1034 nuclei, using masks manually segmented from corresponding brightfield images (code -
1035 Segmentation: *mask2seg*). All analysis was restricted to the image region of effectively
1036 uniform laser illumination (80% ± 9% s.d. peak irradiance) no greater than 190 × 300 pixels
1037 (10 × 16 µm). Each fluorescence sequence was then processed independently (code -
1038 Tracking: *trackAllFields*). For each subsequent frame, the local fluorescence maxima—foci—
1039 were identified, and their intensity estimated, by integrating the pixel value intensity within
1040 5 pixels, and subtracting a background level averaged over the remainder of a 17 × 17-pixel
1041 sliding window. Each of the foci was assigned a signal-to-noise ratio (SNR) equal to its
1042 intensity divided by the standard deviation of the associated background region. Foci above
1043 an initial, permissive SNR threshold of 0.2 were tentatively accepted. These foci were
1044 refined to subpixel precision with an elliptical Gaussian masking algorithm. This returned
1045 fitted estimates of their semi-axes, which reflected the widefield spatial resolution plus out-
1046 of-plane defocus and any residual motion blur. These widefield dimensions (Supplementary
1047 Fig. 12) are close to laterally isotropic and insensitive to stoichiometry, since all the
1048 assemblies are expected to be much smaller than the diffraction limit and to rotate rapidly
1049 relative to the exposure time. The centroids of the foci were also estimated to super-
1050 resolved localisation precision [93] of typically 45–80 nm (Supplementary Fig. 12) but as low as
1051 40 nm for bright assemblies, consistent with best Slimfield performance [96]. For each image
1052 sequence, pairs of foci were then linked consecutively into tracks if their centroids lay within
1053 8 pixels, with width and intensity ratios in the ranges 0.5–2 and 0.5–3 respectively. When
1054 multiple links were possible, the nearest suitable neighbour was chosen.

1055 We then performed sifting of foci and tracks (code - Analysis: *analyseAllTracks*), retaining
1056 only those above a strict SNR threshold and minimum number of frames, respectively. The
1057 first sifting criterion - an SNR threshold - was robustly determined as the SNR value at which
1058 true and false positives occur at equal frequency in a positive control that contains only
1059 single molecules; the false positive rate is estimated from negative controls containing only
1060 noise. For negative controls, we tracked acquisitions of dark noise (zero excitation
1061 intensity), as well as image stacks of simulated noise based on the autofluorescence level
1062 measured in wild-type root tips at the typical excitation intensity (Supplementary Fig. 4).
1063 Prior works recommend a sifting SNR threshold of 0.4 [89,90,97]; here, we found the
1064 appropriate SNR threshold was largely independent of excitation intensity in the kW/cm^2
1065 range and instead determined by two factors: the autofluorescence relative to the
1066 characteristic molecular brightness (Supplementary Fig. 4), and the detector noise. The
1067 actual SNR threshold used ranged from 0.35 for the Prime 95B (12-bit Sensitivity) to 0.50 for
1068 the Prime BSI 16-bit mode (Supplementary Fig. 2c).

1069 Even with accurate distinction of foci from background noise, random overlap between
1070 tracks increases at high emitter density, leading to spurious summation of their intensities.
1071 Noting the temporal correlations present only in real signals, we further strengthened the
1072 sifting procedure with a second criterion: we retained only tracks containing at least 3
1073 consecutive foci. This second criterion reduced the true positive detection rate to 35–50%
1074 (code – Analysis*: plotTrackFrequency*) but increased the positive predictive value (the mean
1075 probability that sifted tracks were correctly identified) from <70% to >95% for single YFP

molecules *in vitro* (Supplementary Fig. 2d). Controls similarly indicate a positive predictive value of >90% for dimers and higher assemblies *in planta* (Supplementary Fig. 2g).

To understand the impact of higher particle densities, we estimated the theoretical probability of random overlap between tracks using a continuum model [89], which estimates the probability of nearest neighbour distances in a random Poisson process falling within the widefield localisation precision. According to this model, the expected fraction of randomly overlapping tracks retained after sifting was <10% for all cases in this study. Conversely for extremely low densities, the higher the SNR threshold is set, the brighter false positives will appear when they do eventually arise. This can be problematic when the true positive rate is very low, for example when estimating characteristic molecular brightness at very low emitter density.

The 2D diffusivity of each track was estimated according to a random walk model as a quarter of the rate of increase of the mean-squared displacement with lag time [98] (code – Analysis*: plotDiffusivity*).

The initial intensity of each track was determined by backward extrapolation of the intensities of its first 5 foci to a virgin timepoint prior to photobleaching.

The characteristic molecular brightness of each fluorescent reporter species was determined based on the Chung-Kennedy-filtered [99,100] terminal intensity of tracks in each acquisition (Supplementary Fig. 1, code – Characteristic Molecular Brightness: *overTrackAll*, *CKfilterBaseline, plotOverTracks*). After calibration, at 10 ms exposure time in plant nuclei at 20 µm working depth, the characteristic molecular brightness was:

VIN3-GFP:	103 ± 9 photons (172 ± 15 counts, mean ± sem),
VRN5-YFP and LacI-YFP:	76 ± 10 photons (126 ± 16 counts),
VIN3-SYFP2:	79 ± 15 photons (131 ± 25 counts) and
VRN5-mScarlet-I:	84 ± 11 photons (140 ± 18 counts).

Previous Slimfield work gives comparable values ranging from 60–250 photons per frame, albeit for fluorescent proteins within 1 µm from the coverslip surface [61,89,48]. For a quantitative comparison at greater working depths, *in vitro* values were obtained from recombinant YFP on a tilted surface under the same SlimVar imaging conditions (Supplementary Fig. 2f). The drops in characteristic molecular brightness imply photon collection losses of 25% over the working depth, compared to 30% in the root tissue itself. This corresponds to an average emission decay length in tissue of about 60 µm, which limits the range of working depths across which a given characteristic molecular brightness value can be used within error, to ± 10 µm.

The internally calibrated values listed above were then used to normalise intensity metrics into numbers of labelled molecules. First, the number of molecules associated with each tracked assembly – its **stoichiometry** – is the initial track intensity divided by the characteristic molecular brightness (code – Analysis*: plotStoichiometry*). The same normalisation factor is used for each dataset's stoichiometry **periodicity**, as well as its **total protein number**.

1116 ## Autofluorescence and total protein number

1117 Raw estimates of the total number of molecules in each nucleus were extracted with an
1118 *ImageJ* macro following [45] (code – Total Protein Number: *MonoCropper.ijm*); the pixel values
1119 were integrated within each nuclear segment, then normalised by the characteristic
1120 molecular brightness to give an integrated nuclear intensity in molecular equivalents
1121 (Fig. 4a). These values did not account for the additive contribution from autofluorescence
1122 background, which we estimated using the corresponding unlabelled control line, Col*FRI*.
1123 The total protein number of each labelled dataset was refined to exclude autofluorescence
1124 by taking the difference between mean integrated nuclear intensities of the labelled dataset
1125 and unlabelled control, adjusted in proportion to the ratio of mean areas of nuclear
1126 segments. The negative control was much brighter in green acquisitions (15,000 ± 1500 GFP
1127 equivalents, or 1.5×10^6 photons, vs. 3,800 ± 400 YFP/SYFP2, or 2.8×10^5 photons; mean ±
1128 sem, N=33, N=27 respectively). The nucleoplasmic concentrations were estimated by
1129 dividing each total protein number by the mean nuclear volume (assuming prolate
1130 spheroidal nuclei aligned in the image plane) and multiplying by Avogadro's number.

1131 We quantified the mean autofluorescence intensity of nuclei in wild-type control (Col*FRI*) as
1132 45 and 26 photons/pixel for 488 nm and 514 nm wavelength excitation (n=250 and 71
1133 nuclei) respectively. We show that this is not prohibitive for SlimVar in these tissues by
1134 considering our SNR metric: if we divide the 103 or 76 photons from a single molecule
1135 (characteristic molecular brightness of GFP or YFP respectively) over the average area of 30
1136 pixels per foci, then divide by the square root of this autofluorescence level, we find
1137 expected signal-to-noise ratios of 0.52 and 0.50, which correspond very well to the empirical
1138 SNR thresholds 0.35-0.50 used in sifting the single molecules from noise. At the 95th
1139 percentile of autofluorescence (109 and 114 photons/pixel), this typical single molecule SNR
1140 reduces to 0.24 and 0.33, reflecting the few adverse cases where only oligomers, and not
1141 single molecules, can be detected reliably. However, the stoichiometry of those oligomers
1142 can still be precisely counted with characteristic molecular brightness obtained elsewhere in
1143 regions of sufficiently low local autofluorescence.

1144 ## Stoichiometry periodicity analysis

1145 To calculate stoichiometry periodicity (code – Analysis: *plotNearestNeighbourPeriodicity*),
1146 first the stoichiometries of all tracks within each nucleus were aggregated across nuclei in a
1147 dataset (genotype and vernalisation status), then represented as a kernel density
1148 distribution. The choice of the kernel width is informed by the empirical variation in the
1149 characteristic molecular brightness. The observed range is typically ± 30%, i.e. a width of 0.6
1150 molecules in each frame at the SNR threshold [43], but to avoid oversmoothing during the
1151 periodicity analysis, we used the standard error of ± 14%, i.e. 0.3 molecules. Peaks in this
1152 distribution were detected using the MATLAB *findpeaks* function, and the intervals between
1153 nearest neighbour peaks were calculated. The uncertainty in peak-to-peak interval was
1154 estimated as the single-molecule uncertainty of 0.6 molecules multiplied by the square root
1155 of the mean stoichiometry, divided by the square root of the number of interpolated
1156 intervals [91]. To suppress noise and spurious intra-peak sampling, all peak intervals smaller
1157 than the interval uncertainty were discarded. A second kernel density estimate was
1158 calculated over the remaining peak intervals, with the interval uncertainty as the kernel

1159 width. This curve describes the distribution of peak intervals in the stoichiometry as shown
1160 in Fig. 5 (insets) and Supplementary Fig. 11d. The modal value of this interval distribution
1161 was reported as the predominant periodicity of assemblies in each dataset. This method of
1162 estimating periodicity was verified as independent of the mean stoichiometry using
1163 simulated positive control data drawn from noisy Poisson-distributed multiples of an
1164 oligomeric ground truth [48]. This analysis reproduced the expectation that the minimum
1165 number of tracks required for sufficient peak sampling, and therefore the limit of periodicity
1166 detection, scales with the square root of the mean stoichiometry. To demonstrate a
1167 negative control (code – Analysis: *simulateControlPeriodicity*), 100 aperiodic sets of 10^4
1168 stoichiometry values, uniformly distributed at random between 1–30 molecules, were
1169 generated using the *randperm* MATLAB function and processed to generate a set of 100
1170 independent interval distribution curves each corresponding to null periodicity. The 95th
1171 percentile fraction of peak intervals was calculated at each interval size to generate a null
1172 curve, below which test data could no longer be considered periodic. The uncertainty in the
1173 reported modal peak interval was estimated as the s.e.m. of the peak intervals falling within
1174 the range above the null threshold line. To avoid undersampling the peaks, a minimum
1175 number of tracks were needed: at least 14 multiplied by the mean stoichiometry. Where
1176 necessary, stoichiometry lists from different replicates were aggregated to provide more
1177 robust datasets for periodicity analysis. The variation of periodicity for each individual
1178 replicate may be estimated by bootstrapping pairs of replicates together to meet the
1179 threshold number of tracks. The periodicity analysis was validated *in vivo* using the
1180 standard of tetrameric LacI-YFP [65] detected in the *FLC-lacO*/LacI-YFP lines (Supplementary
1181 Fig. 10b).

1182 Two-colour imaging and colocalisation

1183 For each nucleus, a z-stack was performed, first with brightfield imaging to ensure
1184 alignment, then with 514 nm wavelength SlimVar excitation at 10 ms/frame exposure to
1185 track *FLC* loci via LacI-YFP. This z-range extended from the highest to lowest surface of each
1186 nucleus with respect to the coverslip surface and was divided into equally spaced intervals
1187 of 280–360 nm. During each stack, the z-position of the image frame (denoted I*)
1188 containing the brightest LacI-YFP foci was noted and subsequently revisited (Fig. 7a). We
1189 then performed a dual-colour SlimVar acquisition, 10 ms exposure time alternating between
1190 561 nm and 514 nm excitation wavelengths to facilitate distinct signals for each reporter
1191 free from bleed-through. The total duration of the fluorescent z-stack and alternating
1192 excitation acquisitions for each nucleus was ≤15 s. We estimate that the maximum
1193 displacement of *FLC* loci during the 15 s period was within 180 nm, less than our optical
1194 resolution limit (Supplementary Fig. 12d) and consistent with previous observations,[101] thus
1195 in effect immobile over this timescale.
1196 During post-processing, the two colour channels were spatially aligned to sub-pixel precision
1197 using affine transforms generated from SlimVar images of 200 nm diameter fluorescent
1198 beads *in vitro* (code - Alignment: *generateBeadTransform*). Then both yellow and red
1199 channel image sequences were tracked independently (Fig. 7b) to generate lists of LacI-YFP
1200 and VRN5-mScI tracks respectively. To account for *FLC* candidates observed in the z-stack

1201 but photobleached prior to the alternating acquisition, a copy of the alternating sequence
1202 was generated in which each yellow channel image simply comprised I*. This copy was also
1203 tracked, and its list of LacI-YFP tracks appended to the list from the original sequence.
1204 Collected LacI-YFP tracks are shown in Fig. 7b (yellow traces).
1205 To exclude false positive detections of *FLC* due to free LacI-YFP, we then selected only slow
1206 and bright yellow tracks. Our earlier observations suggest a maximum of 8 *FLC* loci in the
1207 entire nucleus (Supplementary Fig. 9). On that basis, we selected the LacI-YFP tracks whose
1208 diffusivity was ≤ D_{FLC} (Fig. 6a) and from these, retained the 8 brightest (or all if fewer than 8)
1209 tracks in each nucleus. These selected *FLC* tracks, typically 1–4 per nucleus (Fig. 7b, white
1210 circles), were run through colocalisation analysis (code – Analysis: *analyseAllTracks*) with the
1211 corresponding VRN5-mScI tracks (Fig. 7b, magenta traces) using a previously reported
1212 algorithm [89]. Briefly, VRN5 and *FLC* tracks were deemed colocalised if they met an intensity
1213 overlap condition [102] of at least 50% (effectively a lateral distance of ~3 pixels or one
1214 widefield localisation precision) and remained within a distance of 7 pixels (twice the
1215 widefield localisation precision) for ≥3 frames. The high numerical aperture and short depth
1216 of field ensured an axial precision better than <220 nm FWHM for all colocalisations. The
1217 likelihood of false positive overlaps between VRN5 tracks, and the likelihood of false
1218 positive colocalisations (an *FLC* locus being colocalised with a VRN5 assembly by random
1219 chance) were both <5%, based on the average initial number density of tracks in each frame
1220 (5.2 VRN5 and 3.3 candidate *FLC*) distributed in the nucleoplasm under random point
1221 statistics [103]. The residence time of each colocalised track was determined from the number
1222 of adjacent colocalised frames [70] (code – Analysis: *plotResidenceTimes*).

1223 Statistics and samples

1224 Comparisons of the frequency of colocalised assemblies (Fig. 7d) used Fisher's exact test
1225 (two-tailed). All other pairwise comparisons used the non-parametric Brunner-Munzel test
1226 (code – Analysis: *BrunnerMunzelTest*). Sample size and significance are indicated alongside
1227 each result. Investigators were not blinded and each acquisition was independent. We
1228 predetermined a target sample size of >24 cells total per line per condition, sufficiently
1229 powered to detect changes of <1 s.d. in each of the five test variables (number of tracks,
1230 total protein number, stoichiometry, periodicity, diffusivity) at a Bonferroni-adjusted
1231 significance level of $\alpha = 0.05/5 = 0.01$. We planned biological replicates of >3 independent
1232 cycles of growth and vernalisation, with >3 roots per cycle and >3 cells per root. In the dual
1233 line, >10 cells per condition sufficed for estimates of track number and stoichiometry
1234 disaggregated by colocalisation. Technical replicates were identified with tracks detected
1235 within each nuclear segment. Actual numbers of replicates analysed are detailed in
1236 Supplementary Table 2.

1237

1238 Data and Code Availability

1239 All raw and processed imaging data and analysed tracks are available at the BioImage
1240 Archive: https://doi.org/10.6019/S-BIAD1217. ADEMScode v2.2 software for tracking
1241 analysis in MATLAB, and the corresponding documentation and exemplar data, can be
1242 found at https://github.com/alex-payne-dwyer/single-molecule-tools-alpd.

1243 # References

1244

1245 1 Johnstone SE, Gladyshev VN, Aryee MJ, Bernstein BE. Epigenetic clocks, aging, and cancer.
1246 *Science* 2022; **378**: 1276–1277.

1247 2 Varotto S, Tani E, Abraham E, Krugman T, Kapazoglou A, Melzer R *et al.* Epigenetics: possible
1248 applications in climate-smart crop breeding. *Journal of Experimental Botany* 2020; **71**: 5223–
1249 5236.

1250 3 Cavalli G, Heard E. Advances in epigenetics link genetics to the environment and disease. *Nature*
1251 2019; **571**: 489–499.

1252 4 Zetzsche J, Fallet M. To live or let die? Epigenetic adaptations to climate change—a review.
1253 *Environ Epigenet* 2024; **10**: dvae009.

1254 5 Müller J, Kassis JA. Polycomb response elements and targeting of Polycomb group proteins in
1255 Drosophila. *Curr Opin Genet Dev* 2006; **16**: 476–484.

1256 6 Coleman RT, Struhl G. Causal role for inheritance of H3K27me3 in maintaining the off state of a
1257 Drosophila HOX gene. *Science* 2017; **356**: eaai8236.

1258 7 Blackledge NP, Klose RJ. The molecular principles of gene regulation by Polycomb repressive
1259 complexes. *Nat Rev Mol Cell Biol* 2021; **22**: 815–833.

1260 8 Menon G, Schulten A, Dean C, Howard M. Digital paradigm for Polycomb epigenetic switching
1261 and memory. *Curr Opin Plant Biol* 2021; **61**: 102012.

1262 9 Hepworth J, Antoniou-Kourounioti RL, Bloomer RH, Selga C, Berggren K, Cox D *et al.* Absence of
1263 warmth permits epigenetic memory of winter in Arabidopsis. *Nature Communications* 2018; **9**:
1264 639.

1265 10 Antoniou-Kourounioti RL, Hepworth J, Heckmann A, Duncan S, Qüesta J, Rosa S *et al.*
1266 Temperature Sensing Is Distributed throughout the Regulatory Network that Controls FLC
1267 Epigenetic Silencing in Vernalization. *Cell Systems* 2018; **7**: 643–655.

1268 11 Yang H, Berry S, Olsson TSG, Hartley M, Howard M, Dean C. Distinct phases of Polycomb
1269 silencing to hold epigenetic memory of cold in Arabidopsis. *Science* 2017; **357**: 1142–1145.

1270 12 Angel A, Song J, Yang H, Questa JI, Dean C, Howard M. Vernalizing cold is registered digitally at
1271 FLC. *Proc Natl Acad Sci U S A* 2015; **112**: 4146–4151.

1272 13 Costa S, Dean C. Storing memories: The distinct phases of Polycomb-mediated silencing of
1273 Arabidopsis FLC. *Biochemical Society Transactions* 2019; **47**: 1187–1196.

1274 14 Berry S, Hartley M, Olsson TSG, Dean C, Howard M. Local chromatin environment of a Polycomb
1275 target gene instructs its own epigenetic inheritance. *eLife* 2015; **4**: e07205.

1276 15 Mylne JS, Barrett L, Tessadori F, Mesnage S, Johnson L, Bernatavichute YV *et al.* LHP1, the
1277 Arabidopsis homologue of HETEROCHROMATIN PROTEIN1, is required for epigenetic silencing of

1278 FLC. *Proceedings of the National Academy of Sciences of the United States of America* 2006; **103**:
1279 5012–7.

1280 16 Saxton DS, Rine J. Epigenetic memory independent of symmetric histone inheritance. *eLife* 2019;
1281 **8**: 1–44.

1282 17 Lövkvist C, Mikulski P, Reeck S, Hartley M, Dean C, Howard M. Hybrid protein assembly-histone
1283 modification mechanism for PRC2-based epigenetic switching and memory. *eLife* 2021; **10**:
1284 e66454.

1285 18 Laugesen A, Højfeldt JW, Helin K. Molecular Mechanisms Directing PRC2 Recruitment and H3K27
1286 Methylation. *Molecular Cell* 2019; **74**: 8–18.

1287 19 Greb T, Mylne JS, Crevillen P, Geraldo N, An H, Gendall AR *et al.* The PHD Finger Protein VRN5
1288 Functions in the Epigenetic Silencing of Arabidopsis FLC. *Current Biology* 2007; **17**: 73–78.

1289 20 Sung S, Amasino RM. Vernalization in Arabidopsis thaliana is mediated by the PHD finger protein
1290 VIN3. *Nature* 2004; **427**: 159–64.

1291 21 Franco-Echevarría E, Rutherford TJ, Fiedler M, Dean C, Bienz M. Plant vernalization proteins
1292 contain unusual PHD superdomains without histone H3 binding activity. *Journal of Biological*
1293 *Chemistry* 2022; **298**. doi:10.1016/j.jbc.2022.102540.

1294 22 Kim DH, Sung S. Coordination of the vernalization response through a VIN3 and FLC gene family
1295 regulatory network in Arabidopsis. *Plant Cell* 2013; **25**: 454–69.

1296 23 Fiedler M, Franco-Echevarría E, Schulten A, Nielsen M, Rutherford TJ, Yeates A *et al.* Head-to-tail
1297 polymerization by VEL proteins underpins cold-induced Polycomb silencing in flowering control.
1298 *Cell Rep* 2022; **41**: 111607.

1299 24 Hepler PK, Gunning BES. Confocal fluorescence microscopy of plant cells. *Protoplasma* 1998;
1300 **201**: 121–157.

1301 25 Shaw SL, Thoms D, Powers J. Structured illumination approaches for super-resolution in plant
1302 cells. *Microscopy (Oxf)* 2019; **68**: 37–44.

1303 26 Ovecka M, Sojka J, Tichá M, Komis G, Basheer J, Marchetti C *et al.* Imaging plant cells and organs
1304 with light-sheet and super-resolution microscopy. *Plant Physiology* 2022; **188**: 683–702.

1305 27 Guo AY, Zhang YM, Wang L, Bai D, Xu YP, Wu WQ. Single-molecule imaging in living plant cells: A
1306 methodological review. *International Journal of Molecular Sciences* 2021; **22**: 5071.

1307 28 Dumur T, Duncan S, Graumann K, Desset S, Randall RS, Scheid M *et al.* Probing the 3D
1308 architecture of the plant nucleus with microscopy approaches: challenges and solutions. *Nucleus*
1309 2019; **10**: 181–212.

1310 29 Colin L, Martin-Arevalillo R, Bovio S, Bauer A, Vernoux T, Caillaud MC *et al.* Imaging the living
1311 plant cell: From probes to quantification. *Plant Cell* 2022; **34**: 247–272.

1312 30 Wang X, Li X, Deng X, Luu DT, Maurel C, Lin J. Single-molecule fluorescence imaging to quantify
1313 membrane protein dynamics and oligomerization in living plant cells. *Nature Protocols* 2015; **10**:
1314 2054–63.

1315 31 Cui Y, Yu M, Yao X, Xing J, Lin J, Li X. Single-Particle Tracking for the Quantification of Membrane
1316 Protein Dynamics in Living Plant Cells. *Molecular Plant* 2018; **11**: 1315–1327.

1317 32 Prunet N, Duncan K. Imaging flowers: a guide to current microscopy and tomography techniques
1318 to study flower development. *Journal of Experimental Botany* 2020; **71**: 2898–2909.

1319 33 Platre MP, Bayle V, Armengot L, Bareille J, Marquès-Bueno M del M, Creff A *et al.*
1320 Developmental control of plant Rho GTPase nano-organization by the lipid phosphatidylserine.
1321 *Science* 2019; **364**: 57–62.

1322 34 Zhang X, Cui Y, Yu M, Lin J. Single-Molecule Techniques for Imaging Exo-Endocytosis Coupling in
1323 Cells. *Trends Plant Sci* 2019; **24**: 879–880.

1324 35 Chen B-C, Legant WR, Wang K, Shao L, Milkie DE, Davidson MW *et al.* Lattice light-sheet
1325 microscopy: Imaging molecules to embryos at high spatiotemporal resolution. *Science* 2014;
1326 **346**: 1257998.

1327 36 Liu T-L, Upadhyayula S, Milkie DE, Singh V, Wang K, Swinburne IA *et al.* Observing the cell in its
1328 native state: Imaging subcellular dynamics in multicellular organisms. *Science* 2018; **360**:
1329 eaaq1392.

1330 37 Schmidt R, Weihs T, Wurm CA, Jansen I, Rehman J, Sahl SJ *et al.* MINFLUX nanometer-scale 3D
1331 imaging and microsecond-range tracking on a common fluorescence microscope. *Nat Commun*
1332 2021; **12**: 1478.

1333 38 Deguchi T, Iwanski MK, Schentarra E-M, Heidebrecht C, Schmidt L, Heck J *et al.* Direct
1334 observation of motor protein stepping in living cells using MINFLUX. *Science* 2023; **379**: 1010–
1335 1015.

1336 39 Bayle V, Fiche JB, Burny C, Platre MP, Nollmann M, Martinière A *et al.* Single-particle tracking
1337 photoactivated localization microscopy of membrane proteins in living plant tissues. *Nature*
1338 *Protocols* 2021; **16**: 1600–1628.

1339 40 Lummer M, Humpert F, Wiedenlübbert M, Sauer M, Schüttpelz M, Staiger D. A New Set of
1340 Reversibly Photoswitchable Fluorescent Proteins for Use in Transgenic Plants. *Molecular Plant*
1341 2013; **6**: 1518–1530.

1342 41 Iwatate RJ, Yoshinari A, Yagi N, Grzybowski M, Ogasawara H, Kamiy M *et al.* Covalent Self-
1343 labeling of tagged proteins with chemical fluorescent dyes in BY-2 cells and arabidopsis
1344 seedlings. *Plant Cell* 2020; **32**: 3081–3094.

1345 42 Yagi N, Yoshinari A, Iwatate RJ, Isoda R, Frommer WB, Nakamura M. Advances in Synthetic
1346 Fluorescent Probe Labeling for Live-Cell Imaging in Plants. *Plant and Cell Physiology* 2021; **62**:
1347 1259–1268.

1348 43 Leake MC, Chandler JH, Wadhams GH, Bai F, Berry RM, Armitage JP. Stoichiometry and turnover
1349 in single, functioning membrane protein complexes. *Nature* 2006; **443**: 355–358.

1350 44 Plank M, Wadhams GH, Leake MC. Millisecond timescale slimfield imaging and automated
1351 quantification of single fluorescent protein molecules for use in probing complex biological
1352 processes. *Integrative Biology* 2009; **1**: 602–612.

1353 45 Wollman AJM, Leake MC. Millisecond single-molecule localization microscopy combined with
1354 convolution analysis and automated image segmentation to determine protein concentrations
1355 in complexly structured, functional cells, one cell at a time. *Faraday Discussions* 2015; **184**: 401–
1356 424.

1357 46 Miller H, Cosgrove J, Wollman AJM, Taylor E, Zhou Z, O'Toole PJ *et al.* High-speed single-
1358 molecule tracking of CXCL13 in the B-follicle. *Frontiers in Immunology* 2018; **9**: 1073.

1359 47 Shashkova S, Wollman A, Hohmann S, Leake MC. Characterising Maturation of GFP and mCherry
1360 of Genomically Integrated Fusions in Saccharomyces cerevisiae. *Bio-Protocol* 2018; **8**: e.2710.

1361 48 Payne-Dwyer AL, Syeda AH, Shepherd JW, Frame L, Leake MC. RecA and RecB: probing
1362 complexes of DNA repair proteins with mitomycin C in live Escherichia coli with single-molecule
1363 sensitivity. *Journal of The Royal Society Interface* 2022; **19**: 20220437.

1364 49 Dresser L, Hunter P, Yendybayeva F, Hargreaves AL, Howard JAL, Evans GJO *et al.* Amyloid-β
1365 oligomerization monitored by single-molecule stepwise photobleaching. *Methods* 2021; **193**:
1366 80–95.

1367 50 Konopka CA, Bednarek SY. Variable-angle epifluorescence microscopy: A new way to look at
1368 protein dynamics in the plant cell cortex. *Plant Journal* 2008; **53**: 186–96.

1369 51 Tokunaga M, Imamoto N, Sakata-Sogawa K. Highly inclined thin illumination enables clear single-
1370 molecule imaging in cells. *Nature Methods* 2008; **5**: 159–61.

1371 52 Gardini L, Vignolini T, Curcio V, Pavone FS, Capitanio M. Optimization of highly inclined
1372 illumination for diffraction-limited and super-resolution microscopy. *Opt Express* 2023; **31**:
1373 26208–26225.

1374 53 Reihani SNS, Charsooghi MA, Khalesifard HR, Golestanian R. Efficient in-depth trapping with an
1375 oil-immersion objective lens. *Opt Lett* 2006; **31**: 766–768.

1376 54 Reihani SNS, Mir SA, Richardson AC, Oddershede LB. Significant improvement of optical traps by
1377 tuning standard water immersion objectives. *Journal of Optics* 2011; **13**. doi:10.1088/2040-
1378 8978/13/10/105301.

1379 55 Dienerowitz M, Gibson G, Bowman R, Padgett M. Holographic aberration correction: optimising
1380 the stiffness of an optical trap deep in the sample. *Opt Express* 2011; **19**: 24589–24595.

1381 56 Schwertner M, Booth MJ, Wilson T. Simple optimization procedure for objective lens correction
1382 collar setting. *J Microsc* 2005; **217**: 184–187.

1383 57 Ue Y, Monai H, Higuchi K, Nishiwaki D, Tajima T, Okazaki K *et al.* A spherical aberration-free
1384 microscopy system for live brain imaging. *Biochem Biophys Res Commun* 2018; **500**: 236–241.

1385 58 Kubitscheck U, Kückmann O, Kues T, Peters R. Imaging and Tracking of Single GFP Molecules in
1386 Solution. *Biophysical Journal* 2000; **78**: 2170–2179.

1387 59 Zhao Q, Young IT, de Jong JGS. Photon budget analysis for fluorescence lifetime imaging
1388 microscopy. *J Biomed Opt* 2011; **16**: 086007.

1389 60 Qüesta JI, Antoniou-Kourounioti RL, Rosa S, Li P, Duncan S, Whittaker C *et al.* Noncoding SNPs
1390 influence a distinct phase of Polycomb silencing to destabilize long-term epigenetic memory at
1391 Arabidopsis FLC. *Genes and Development* 2020; **34**: 446–461.

1392 61 Payne-Dwyer AL, Leake MC. Single-molecular quantification of flowering control proteins within
1393 nuclear condensates in live whole Arabidopsis root. In: Leake MC (ed). *Chromosome*
1394 *Architecture: Methods in Molecular Biology*. Springer US, Humana: New York, NY, 2022, p 2476.

1395 62 Dittmer TA, Stacey NJ, Sugimoto-Shirasu K, Richards EJ. LITTLE NUCLEI genes affecting nuclear
1396 morphology in Arabidopsis thaliana. *Plant Cell* 2007; **19**: 2793–2803.

1397 63 Leake MC. Analytical tools for single-molecule fluorescence imaging in cellulo. *Physical*
1398 *Chemistry Chemical Physics* 2014; **16**: 12635–47.

1399 64 Adler L, Lau CS, Shaikh KM, van Maldegem KA, Payne-Dwyer AL, Lefoulon C *et al.* The role of
1400 BST4 in the pyrenoid of Chlamydomonas reinhardtii. *bioRxiv* 2023; : 2023.06.15.545204.

1401 65 Lewis M, Chang G, Horton NC, Kercher MA, Pace HC, Schumacher MA *et al.* Crystal structure of
1402 the lactose operon repressor and its complexes with DNA and inducer. *Science* 1996; **271**: 1247–
1403 1254.

1404 66 Wollman AJM, Syeda AH, Howard JAL, Payne-Dwyer A, Leech A, Warecka D *et al.* Tetrameric
1405 UvrD Helicase Is Located at the E. Coli Replisome due to Frequent Replication Blocks. *J Mol Biol*
1406 2024; **436**: 168369.

1407 67 Rosa S, De Lucia F, Mylne JS, Zhu D, Ohmido N, Pendle A *et al.* Physical clustering of FLC alleles
1408 during polycomb-mediated epigenetic silencing in vernalization. *Genes and Development* 2013;
1409 **27**: 1845–50.

1410 68 Ladouceur A-M, Parmar BS, Biedzinski S, Wall J, Tope SG, Cohn D *et al.* Clusters of bacterial RNA
1411 polymerase are biomolecular condensates that assemble through liquid-liquid phase separation.
1412 *Proc Natl Acad Sci U S A* 2020; **117**: 18540–18549.

1413 69 Bindels DS, Haarbosch L, van Weeren L, Postma M, Wiese KE, Mastop M *et al.* mScarlet: a bright
1414 monomeric red fluorescent protein for cellular imaging. *Nat Methods* 2017; **14**: 53–56.

1415 70 Stracy M, Wollman AJM, Kaja E, Gapinski J, Lee JE, Leek VA *et al.* Single-molecule imaging of DNA
1416 gyrase activity in living Escherichia coli. *Nucleic Acids Research* 2019; **47**: 210–220.

1417 71 Zhan H, Stanciauskas R, Stigloher C, Keomanee-Dizon K, Jospin M, Bessereau J-L *et al.* In vivo
1418 single-molecule imaging identifies altered dynamics of calcium channels in dystrophin-mutant C.
1419 elegans. *Nat Commun* 2014; **5**: 4974.

1420 72 Ritter JG, Veith R, Veenendaal A, Siebrasse JP, Kubitscheck U. Light Sheet Microscopy for Single
1421 Molecule Tracking in Living Tissue. *PLOS ONE* 2010; **5**: e11639.

1422 73 Reisser M, Palmer A, Popp AP, Jahn C, Weidinger G, Gebhardt JCM. Single-molecule imaging
1423 correlates decreasing nuclear volume with increasing TF-chromatin associations during zebrafish
1424 development. *Nat Commun* 2018; **9**: 5218.

1425 74 Li X, Wang X, Yang Y, Li R, He Q, Fang X *et al.* Single-Molecule Analysis of PIP2;1 Dynamics and
1426 Partitioning Reveals Multiple Modes of Arabidopsis Plasma Membrane Aquaporin Regulation.
1427 *Plant Cell* 2011; **23**: 3780–3797.

1428 75 Song K, Xue Y, Wang X, Wan Y, Deng X, Lin J. A modified GFP facilitates counting membrane
1429 protein subunits by step-wise photobleaching in *Arabidopsis*. *Journal of Plant Physiology* 2017;
1430 **213**: 129–133.

1431 76 Pain C, Tynan C, Botchway SW, Kriechbaumer V. Variable-Angle Epifluorescence Microscopy for
1432 Single-Particle Tracking in the Plant ER. *Methods Mol Biol* 2024; **2772**: 273–283.

1433 77 von Arx M, Xhelilaj K, Schulz P, zur Oven-Krockhaus S, Gronnier J. Photochromic reversion
1434 enables long-term tracking of single molecules in living plants. 2024; : 2024.04.10.585335.

1435 78 Rohr L, Ehinger A, Rausch L, Glöckner Burmeister N, Meixner AJ, Gronnier J *et al.* OneFlowTraX: a
1436 user-friendly software for super-resolution analysis of single-molecule dynamics and nanoscale
1437 organization. *Front Plant Sci* 2024; **15**. doi:10.3389/fpls.2024.1358935.

1438 79 Tang J, Han KY. Extended field-of-view single-molecule imaging by highly inclined swept
1439 illumination. *Optica* 2018; **5**: 1063.

1440 80 Ren J, Han KY. 2.5D Microscopy: Fast, High-Throughput Imaging via Volumetric Projection for
1441 Quantitative Subcellular Analysis. *ACS Photonics* 2021; **8**: 933–942.

1442 81 Wollman AJM, Hedlund EG, Shashkova S, Leake MC. Towards mapping the 3D genome through
1443 high speed single-molecule tracking of functional transcription factors in single living cells.
1444 *Methods* 2020; **170**: 82–89.

1445 82 Miura N, Ashida Y, Matsuda Y, Shibuya T, Tamada Y, Hatsumi S *et al.* Adaptive Optics Microscopy
1446 with Wavefront Sensing Based on Neighbor Correlation. *Plant and Cell Physiology* 2023; **64**:
1447 1372–1382.

1448 83 Jin X, Lee J-EJE, Schaefer C, Luo X, Wollman AJM, Payne-Dwyer AL *et al.* Membraneless
1449 organelles formed by liquid-liquid phase separation increase bacterial fitness. *Science Advances*
1450 2021; **7**: eabh2929.

1451 84 Schulten A, Jang G-J, Payne-Dwyer A, Nielsen ML, Bienz M, Leake MC *et al.* Functional
1452 specialization of Arabidopsis VEL polymerization domains in the switch to Polycomb silencing.
1453 2024; : 2024.02.15.580496.

1454 85 Qüesta JI, Song J, Geraldo N, An H, Dean C. Arabidopsis transcriptional repressor VAL1 triggers
1455 Polycomb silencing at FLC during vernalization. *Science* 2016; **353**: 485–488.

1456 86 Jones JDG, Shlumukov L, Carland F, English J, Scofield SR, Bishop GJ *et al.* Effective vectors for
1457 transformation, expression of heterologous genes, and assaying transposon excision in
1458 transgenic plants. *Transgenic Research* 1992; **1**: 285–297.

1459 87 Box MS, Coustham V, Dean C, Mylne JS. Protocol: A simple phenol-based method for 96-well
1460 extraction of high quality RNA from Arabidopsis. *Plant Methods* 2011; **7**: 7.

1461 88 Schindelin J, Arganda-Carreras I, Frise E, Kaynig V, Longair M, Pietzsch T *et al.* Fiji: an open-
1462 source platform for biological-image analysis. *Nat Methods* 2012; **9**: 676–682.

1463 89 Syeda AH, Wollman AJM, Hargreaves AL, Howard JAL, Brüning J-G, McGlynn P *et al.* Single-
1464 molecule live cell imaging of Rep reveals the dynamic interplay between an accessory replicative
1465 helicase and the replisome. *Nucleic Acids Research* 2019; **47**: 6287–6298.

1466 90 Shepherd JW, Payne-Dwyer AL, Lee J-E, Syeda A, Leake MC. Combining single-molecule super-
1467 resolved localization microscopy with fluorescence polarization imaging to study cellular
1468 processes. *JPhys Photonics* 2021; **3**. doi:10.1088/2515-7647/ac015d.

1469 91 Hunter P, Payne-Dwyer AL, Shaw M, Signoret N, Leake MC. Single-molecule and super-resolved
1470 imaging deciphers membrane behavior of onco-immunogenic CCR5. *iScience* 2022; **25**: 105675.

1471 92 Grossmann G, Krebs M, Maizel A, Stahl Y, Vermeer JEM, Ott T. Green light for quantitative live-
1472 cell imaging in plants. *Journal of Cell Science* 2018; **131**: jcs209270.

1473 93 Thompson RE, Larson DR, Webb WW. Precise nanometer localization analysis for individual
1474 fluorescent probes. *Biophysical Journal* 2002; **82**: 2775–83.

1475 94 Llorente-Garcia I, Lenn T, Erhardt H, Harriman OL, Liu L-N, Robson A *et al.* Single-molecule in vivo
1476 imaging of bacterial respiratory complexes indicates delocalized oxidative phosphorylation.
1477 *Biochimica et Biophysica Acta (BBA) - Bioenergetics* 2014; **1837**: 811–824.

1478 95 Shepherd JW, Higgins EJ, Wollman AJM, Leake MC. PySTACHIO: Python Single-molecule TrAcking
1479 stoiCHiometry Intensity and simulatiOn, a flexible, extensible, beginner-friendly and optimized
1480 program for analysis of single-molecule microscopy data. *Computational and Structural*
1481 *Biotechnology Journal* 2021; **19**: 4049–4058.

1482 96 Miller H, Zhou Z, Wollman AJM, Leake MC. Superresolution imaging of single DNA molecules
1483 using stochastic photoblinking of minor groove and intercalating dyes. *Methods* 2015; **88**: 81–
1484 88.

1485 97 Lecinski S, Shepherd JW, Bunting K, Dresser L, Quinn SD, MacDonald C *et al.* Correlating viscosity
1486 and molecular crowding with fluorescent nanobeads and molecular probes: in vitro and in vivo.
1487 *Interface Focus* 2022; **12**: 20220042.

1488 98 Robson A, Burrage K, Leake MC. Inferring diffusion in single live cells at the single-molecule
1489 level. *Philosophical Transactions of the Royal Society B: Biological Sciences* 2013; **368**: 20120029.

1490 99 Chung SH, Kennedy RA. Forward-backward non-linear filtering technique for extracting small
1491 biological signals from noise. *Journal of Neuroscience Methods* 1991; **40**: 71–86.

1492 100 Leake MC, Wilson D, Bullard B, Simmons RM, Bubb MR. The elasticity of single kettin
1493 molecules using a two-bead laser-tweezers assay. In: *FEBS Letters*. 2003, pp 55–60.

1494 101 Meschichi A, Rosa S. Visualizing and Measuring Single Locus Dynamics in Arabidopsis
1495 thaliana. In: *Arabidopsis Protocols: Methods in Molecular Biology*. 2021, pp 213–224.

1496 102 Wollman AJM, Fournier C, Llorente-Garcia I, Harriman O, Payne-Dwyer AL, Shashkova S *et al.*
1497 Critical roles for EGFR and EGFR-HER2 clusters in EGF binding of SW620 human carcinoma cells.
1498 *Journal of The Royal Society Interface* 2022; **19**: 20220088.

1499 103 Payne-Dwyer A, Kumar G, Barrett J, Gherman LK, Hodgkinson M, Plevin M *et al.* Predicting
1500 Rubisco-Linker Condensation from Titration in the Dilute Phase. *Phys Rev Lett* 2024; **132**:
1501 218401.

1502 104 Faklaris O, Bancel-Vallée L, Dauphin A, Monterroso B, Frère P, Geny D *et al.* Quality
1503 assessment in light microscopy for routine use through simple tools and robust metrics. *J Cell*
1504 *Biol* 2022; **221**: e202107093.

1505 105 Wilson T. Resolution and optical sectioning in the confocal microscope. *J Microsc* 2011; **244**:
1506 113–121.

1507

1508

Acknowledgements

We would like to thank Ibrahim Cissé and Jamie Hobbs for preliminary discussions, Anna Schulten, Govind Menon, Martin Howard, Pan Zhu, Cecilia Lövkvist, Grant Calder and Aisha Syeda for training and discussions, Mathias Nielsen and Yaoxi Li for generating the VRN5-mScarlet-I and VIN3-SYFP2 constructs, and the Horticulture and Bioscience Technology Facility at the University of York for supporting growth chamber resources and confocal microscopy. Funded by EPSRC (grants EP/T00214X/1, EP/T002166/1 and EP/Y000501/1). For the purpose of open access, a Creative Commons Attribution (CC BY) licence is applied to any Author Accepted Manuscript version arising from this submission.

Author Contributions

Conceptualization, funding acquisition, administration, supervision; ML, CD. Methodology, software and validation: APD, ML; Investigation, data curation, analysis and visualization: APD, GJJ; Writing – original draft preparation: APD; Writing – review & editing: APD, GJJ, CD, ML.

Competing interests

The authors declare no competing interests.

Supplementary Information

Supplementary Table 1. Average stoichiometry of VIN3-GFP, VIN3-SYFP2 and VRN5-YFP assemblies whose diffusivity matches that of *FLC* loci. The diffusivity-matched stoichiometry is distributed similarly to the population (VIN3-SYFP2 V6W, N=296, p=0.08 |ns), and similarly increases with vernalisation for both VIN3 (V2W to V6W, SYFP2: N=262, p<0.001 |**; GFP: N=302, p<0.001 |**) and VRN5 (NV to V6W+T14, N=318, p<0.001 |**). VIN3-SYFP2 values are corrected for the fraction of endogenous VIN3 (Supplementary Fig. 5). NV = not vernalised; V2W = two weeks of cold; V6W = six weeks of cold; V6WT14 = six weeks of cold followed by two weeks of warm conditions.

Line	**Timepoint**	***FLC*-like tracks** $D \approx D_{FLC}$		**Stoichiometry** (molecules)	
		Number	% of total (± s.e.m.)	Median	IQR
VIN3-GFP	V2W	151	15.2 (1.2)	9.9	5.9–16.3
	V6W	262	17.6 (1.1)	15.1	9.0–26.0
VIN3-SYFP2	V2W	131	11.3 (1.0)	3.2	2.0–6.0
				6.4	3.9–11.9 *corrected*
	V6W	148	16.5 (1.4)	5.2	3.8–8.4
				10.4	7.6–16.8 *corrected*
VRN5-YFP	NV	203	18.4 (1.3)	11.3	7.3–23.4
	V2W	168	17.4 (1.3)	17.7	11.1–29.9
	V6W	355	20.8 (1.1)	18.1	11.5–30.2
	V6W+T14	249	19.6 (1.2)	20.4	12.7–31.0

1541 **Supplementary Table 2. Sample statistics used for quantitative SlimVar analysis.** Numbers
1542 of nuclei and tracks quantified**.** Col*FRI* acquisitions were aggregated over all tested
1543 vernalisation conditions: NV = not vernalised; V2W = two weeks of cold; V6W = six weeks of
1544 cold; V6WT7 = six weeks of cold followed by one week of warm conditions; V6WT14 = six
1545 weeks of cold followed by two weeks of warm conditions.

1546

Line	Vernalisation / imaging condition	Independent growth cycles	Cells quantified	Nuclear tracks detected
VIN3-SYFP2	NV	3	22	0
	V2W	4	71	1,158
	V6W	3	46	896
	V6W T7	3	23	0
VIN3-GFP	NV	3	24	0
	V2W	5	57	994
	V6W	4	83	1,485
	V6W T7	4	36	0
VRN5-EYFP	NV	4	50	1,039
	V2W	3	36	964
	V6W	4	63	1,703
	V6W T14	4	54	1,285
VRN5-mScarletI	NV	5	44	552
	V2W	6	29	426
	V6W	2	16	256
	V6W T14	3	29	365
*FLC-lacO/*LacI-YFP	NV	3	38	166
VRN5-mScarletI × *FLC-lacO/*LacI-YFP	NV	3	10	365 × 23
	V2W	2	28	1,703 × 156
	V6W	3	25	2,867 × 192
	V6W T14	2	18	1,416 × 74
Col*FRI*	All (green / 488 nm)	3	79	0
	All (yellow / 514 nm)	3	38	0
	All (red / 561 nm)	3	79	0

1547

1548

1549

1550 **Supplementary Table 3. Primers used in this study.**

Primer name	**Primer sequence 5' -> 3'**
Primers for cloning	
Mega-pENTR VIN3-mTurq2 F	GCGGCAGCTTCAGCCGTGAGCAAGGGCGAGGAG
Mega-pENTR VIN3-mTurq2 R	GAGTTAATAAATAGACCGATTTCAAAAGCTTTTACTTGTACAGCTCGTCCATG
VRN5_mScarlet_T	GCATCCGCGGCAGCTTCAGCCGTGAGCAAGGGCGAGGCA
VRN5_mScarlet_B	GTTGAATCAATGGGAAGCTTGATTACTTGTACAGCTCGTCCATG
qRT-PCR primers	
FP-qPCR-F2	GGACGACGGCAACTACAAGA
FP-qPCR-R2	GTTGCCGTCCTCCTTGAAG
VIN3-qPCR-1F	TGCTTGTGGATCGTCTTGTCA
VIN3-qPCR-1R	TTCTCCAGCATCCGAGCAAG
VRN5_qPCR_F	GAGGCATTGTTAGTAGGCTTCC
VRN5_qPCR_R	CACGCAGCTGGAACTAAATCTC
FLC spliced F	AGCCAAGAAGACCGAACTCA
FLC spliced R	TTTGTCCAGCAGGTGACATC
UBC_qPCR_F	CTGCGACTCAGGGAATCTTCTAA
UBC_qPCR_R	TTGTGCCATTGAATTGAACCC
PP2A F2	ACTGCATCTAAAGACAGAGTTCC
PP2A R2	CCAAGCATGGCCGTATCATGT

1551

1552

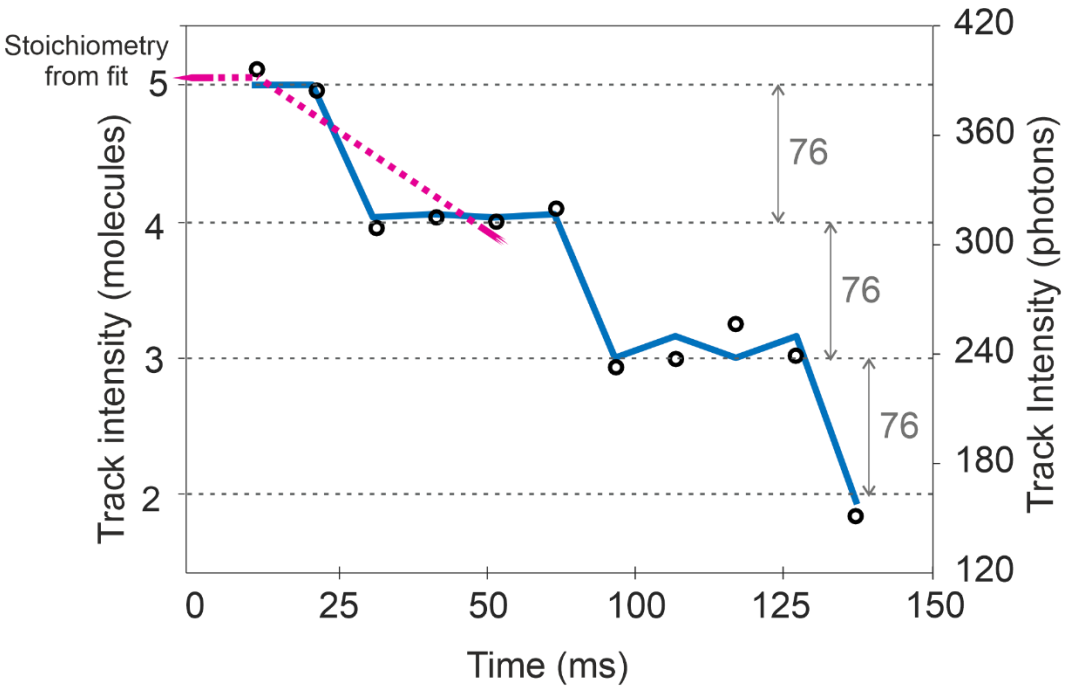

1553

1554 **Supplementary Fig. 1. Determination of characteristic molecular brightness in live tissues**
1555 **from photobleaching.** Intensity of foci (black circles) near the end of a single track in a post-
1556 vernalised VRN5-YFP image sequence, interpolated using a Chung-Kennedy edge-preserving
1557 filter (centred window of 3 points, blue line). With sufficient signal-to-noise, photobleaching
1558 enables counting of individual steps corresponding to the presence of individual labelled
1559 molecules in an assembly. The consistent photobleaching steps from fluorescent fusions
1560 provide enough resolution to count not only molecular steps in specific traces, but also to
1561 derive an ensemble estimate of the characteristic molecular brightness for working depths
1562 of 20 ± 10 µm. The steps yield an estimate of 76 ± 10 photons for the characteristic single-
1563 molecule brightness of the VRN5-YFP fusion *in planta*. Normalisation of the intensity trace
1564 by this value gives the absolute number of active fluorophore reporters over the entire
1565 course of photobleaching, which remains robust when individual steps would be missed or
1566 otherwise unidentifiable. A backward extrapolation of the first five points accounts for
1567 photobleaching and allows thee track stoichiometry to be estimated with better precision
1568 than the individual foci.

1569

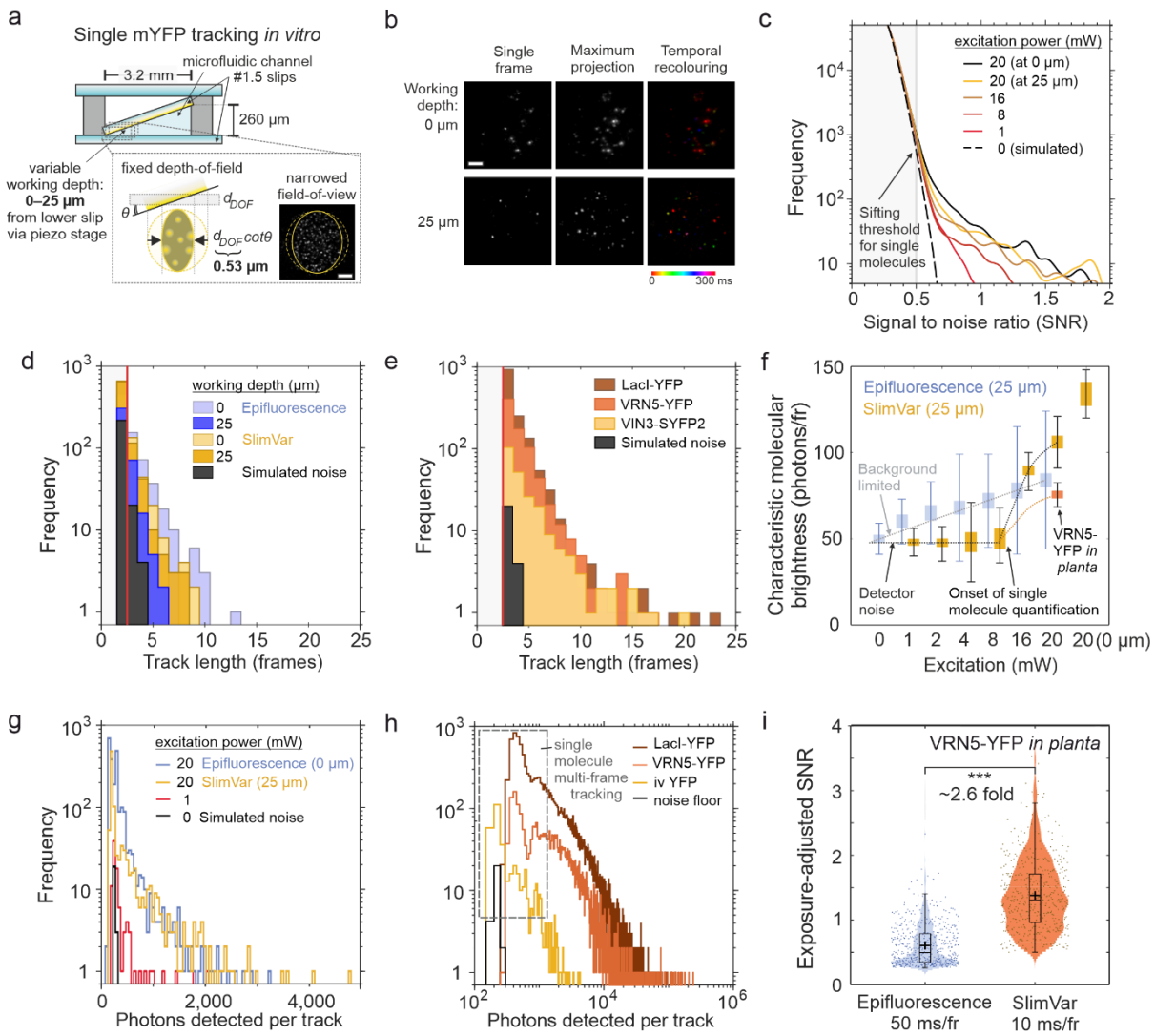

Supplementary Fig. 2, SlimVar detects and quantifies single fluorescent proteins in tracks above threshold levels of excitation power and signal-to-noise. a) A channel with a tilted internal coverslip surface facilitated observation of single particles *in vitro* at a range of working depths. Acquisition and tracking of a purified YFP sample were performed both at zero depth in epifluorescence mode (10 ms exposures) and at a chosen calibration depth of 25 µm in SlimVar mode (10 ms exposures).

If the imaged surface is sufficiently tilted by an angle θ, the depth-of-field (d_{DOF}, the axial extent of the detection volume) limits the width of the region in focus to $d_{DOF}\cot\theta$ (inset scale bar 2 µm). At 25 µm working depth in SlimVar, we found the width to be 6,500 ± 300 nm, thus d_{DOF} = 530 ± 30 nm. At the emission wavelength of 528 nm, this result indicated an effective numerical aperture [104] of 1.38 ± 0.02 (from the nominal NA 1.49), thereby achieving better light collection than possible with any water immersion lens (NA < 1.33).

To create the channel, a 3.2 × 22 mm section of #1.5 coverslip was placed between 5 × 22 mm sections of adhesive spacer of 260 µm depth (125 µL GeneFrame, ThermoFisher) mounted on a standard 25 × 75 mm slide. Additional coverslip sections were added to the

spacers to compensate for the thickness of the tilted slip, before sealing with a final coverslip used for imaging. The formed channel was incubated in 1 µg/ml anti-YFP in phosphate buffer saline (PBS) for 5 min, washed with PBS, followed by 50 nM mYFP in PBS for 5 min, then washed with PBS. For imaging, the channel was placed so that the surface's direction of tilt away from the optical axis was orthogonal to the plane of the beam delivery.

b) Examples of YFP foci observed within a 300 ms window (20 mW excitation, 10 ms exposure per frame), showing similar performance in epifluorescence at zero depth, and in SlimVar at the calibration depth. The temporal recolouring indicates how foci appear (bind), diffuse in short, confined trajectories and disappear (photobleach or unbind); scale bar 2 µm.

c) The appropriate SNR threshold for sifting can be estimated as the SNR above which single molecules are unlikely to be false positives, here at 0.5. This panel shows the frequency distribution of the signal-to-noise metric for individual tracks detected above a nominal capture SNR of 0.2, in 10 fields of view at different excitation powers and working depths after SlimVar calibration: 20 mW power at the coverslip, or zero working depth (solid black), at the calibration working depth of 25 µm at the working excitation powers of 20 mW (yellow) and lower powers of 16 mW (brown), 8 mW (orange) and 1 mW (red). The distribution at zero power is derived from tracking simulations of Gaussian noise matched to the experimental dark detector noise evaluated over three fields of view. This has a standard deviation of 2.3 photons/pixel, which is equivalent to an average background of about 15 photons/pixel.

d) After sifting above the SNR threshold of 0.5, the tracks have a distribution of lengths (number of foci) which varies by modality and working depth. 'Epifluorescence' is performed at 0° beam incidence at 20 mW source power (blue), while 'SlimVar' refers to 60° beam incidence at 20 mW source power after the calibration protocol (yellow). The tracking length for epifluorescence deteriorates with increasing working depth (dark blue vs light blue), while those of SlimVar are less dependent on depth (dark yellow vs light yellow). The tracks of length 3 or more have a much lower overlap with false positives from noise (black), which motivates us to include a minimum track length of 3 in the sifting process.

e) Lengths of tracks detected in plants using SlimVar (LacI-YFP, brown; VRN5-YFP, orange; VIN3-SYFP2, yellow; noise, black). The track lengths for assemblies are correspondingly greater for species with higher mean stoichiometry and lower mean diffusivity.

f) The characteristic molecular brightness, estimated from the mean photons per frame in detected tracks, as a function of excitation power. The detector noise generates a floor value of 50 photons/frame, from the few false positives that inevitably pass the sifting step. For epifluorescence at depth (blue bars), the high background immediately causes the apparent value to increase with excitation power, but for isolated molecules, this is not well correlated with true positive events (panel d). For SlimVar at depth (yellow bars), the background is low and there is a clear onset above a critical power of ~8 mW (irradiance ~4 kW/cm^2) corresponding to the true number of photons detected from a single fluorescent protein. The value is highest at zero working depth (rightmost bar), decreasing slightly at the calibration working depth, and drops further due to scattering and aberrations in plants (orange), yet remains above the floor level.

g) The distribution of the total number of photons associated with each track for optimal epifluorescence at the surface and 20 mW source power (blue), optimal SlimVar at 25 µm working depth and 20 mW source power (yellow), compared with those of SlimVar at 1 mW source power (red), below the requirement for single molecule detection, and the simulated detector noise (black).

h) The total number of photons per track in vivo, plotted on a logarithmic scale (LacI-YFP, brown; VRN5-YFP, orange). In vitro controls are also shown for comparison (single molecule YFP, yellow; noise, black). The total increases for states with high stoichiometry and low diffusivity. Distinct peaks can be seen at low values, corresponding to single molecules integrated over a small discrete number of frames.

i) The signal-to-noise improvement in vivo due to the SlimVar modality for tracks of VRN5-YFP in plants. Epifluorescence is performed at a longer exposure of 50 ms/frame, while SlimVar is at the balanced mode (10 ms/frame). The SNR values shown account for the additional exposure time required by dividing the raw values for epifluorescence by a factor of $(50\ \text{ms}/10\ \text{ms})^{0.5}$. SlimVar detects additional tracks that are lower stoichiometry and higher diffusivity including single molecules, that for epifluorescence would have raw SNR below the sifting threshold of 0.5 and are therefore invisible. Even with epifluorescence showing this bias towards brighter particles, the mean signal-to-noise in SlimVar track is still at least 2.6× greater.

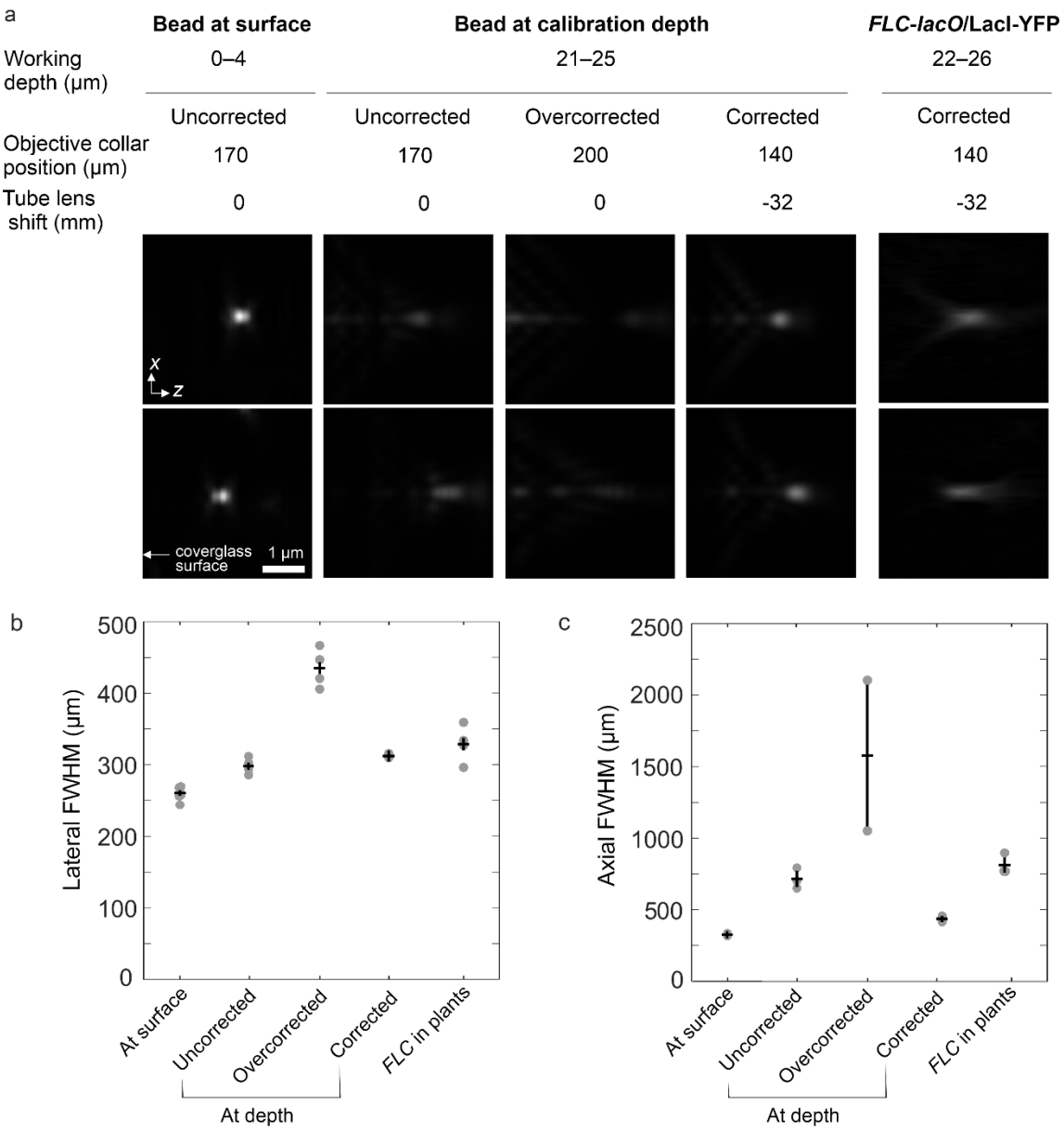

Supplementary Fig. 3. SlimVar sufficiently mitigates aberrations associated with high-numerical aperture imaging at a specified calibration depth.

a) Individual PSFs shown in axial cross section, acquired as volume stacks from either subdiffractive fluorescent beads (24 nm diameter FluoSpheres) suspended in 1 wt.% agarose at 488 nm wavelength excitation at 20 nm z-step, or LacI-YFP foci in root tip nuclei with 514 nm excitation at 250 nm step. Scale bar 1 µm. All PSFs are spatially upsampled to 20 nm (linear interpolation), background-subtracted and normalised to the same total pixel intensity. Top and bottom rows correspond to independent replicate foci. The 'uncorrected state' corresponds to a standard epifluorescence configuration (beam delivery angle of 0° and correction collar set to the coverslip thickness). The 'corrected' state refers to SlimVar including optimal settings of beam delivery angle (60° in water), telescope lens (32 mm towards objective) and correction collar (coverslip thickness - 30 µm). The 'overcorrected' measurement retains the oblique beam delivery angle and standard tube lens position, but

the correction collar is adjusted by an equivalent amount in the opposite direction (coverslip thickness +30 µm) to indicate the impact of the spherical aberration removed in SlimVar. The examples *in planta* are of FLC foci identified in z-stacks (Fig. 7a) using a 'corrected' SlimVar configuration. (b) Lateral and (c) axial FWHM dimensions determined from the PSF volume stacks (n=2–4) using MetroloJ-QC (Image J plugin).[104] The axial FWHMs of beads prior to correction at zero depth, and 'corrected state' at the calibration depth, agree qualitatively with the theoretical diffraction limited resolution [105] of d_z = 0.89 $\lambda/\left(n-\sqrt{n^2-NA^2}\right)$ = 380 nm, and the empirical depth-of-field estimate of 530 nm (Supplementary Fig. 2a) respectively. The axial improvement demonstrated in beads is necessary and sufficient for feasible imaging at depths up to 30 µm inside plant tissue, in which the PSF is subject to additional aberration and scattering.

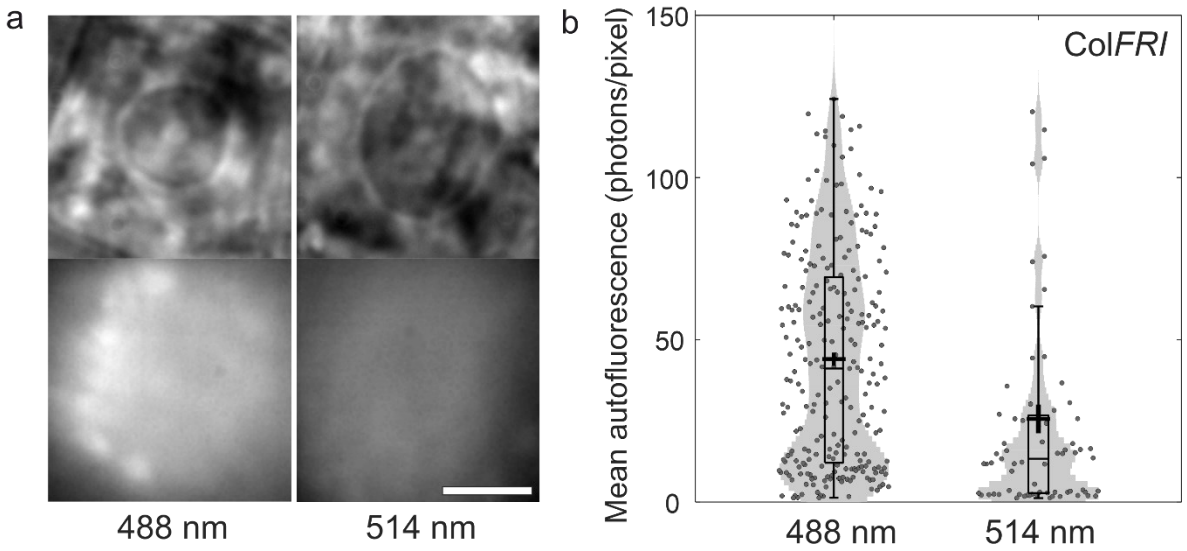

Supplementary Fig. 4. Autofluorescence controls for SlimVar microscopy.

a) SlimVar images of non-vernalised nuclei in the Col*FRI* wild-type (unlabelled) line; top, brightfield; bottom: SlimVar average projections over 100 frames, with contrast set to 120–370 counts (12–162 photons/pixel). Plastids and cell walls have higher autofluorescence than the nucleus, especially at 488 nm (bottom left), but do not contribute to false positives as they are removed during segmentation of the nucleus with the brightfield image. Scale bar: 5 µm. b) The mean number of background fluorescence photons per 53 nm pixel per 10 ms exposure in each nucleus for 488 nm and 514 nm excitation modes, aggregated over all vernalisation timepoints. The mean ± s.e.m. (s.d.) autofluorescence is 45 ± 4 (34) photons/pixel, or 26 ± 4 (33) photons/pixel under 488 nm and 514 nm (n=250 and 71 nuclei) respectively.

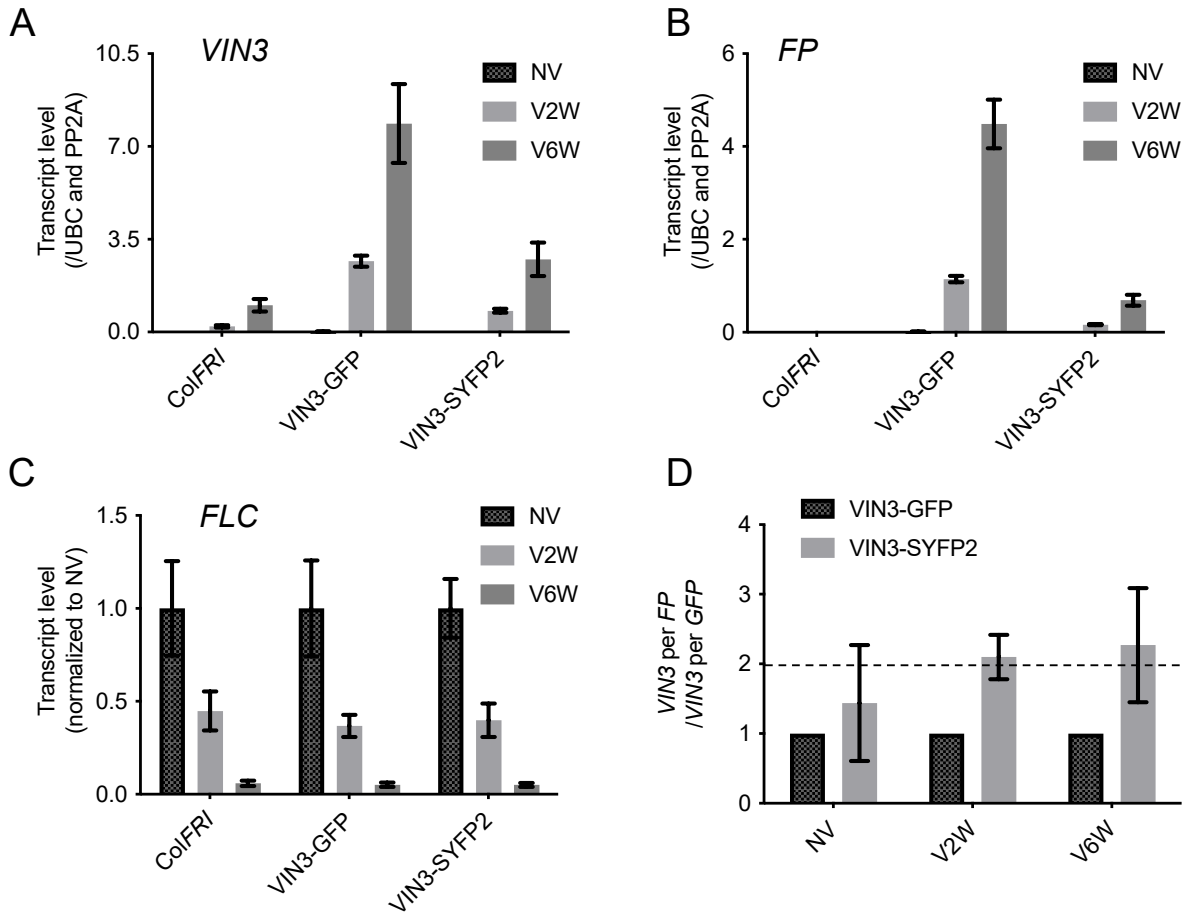

Supplementary Fig. 5. RNA expression analysis and characterization of VIN3-SYFP2.

Expression level of *VIN3* (A), fluorescent protein (B) in VIN3-GFP, VIN3-SYFP2 and Col*FRI* seedlings. (C) Expression level of spliced *FLC* in seedlings after 2 weeks (V2W) and 6 weeks vernalised (V6W) cold seedlings relative to non-vernalised (NV) seedlings. (A-C) Data are presented as mean ± s.e.m. (N=9) from three biologically independent experiments. (D) Based on the assumption that protein levels scale proportionally with RNA levels, we derive a correction factor to infer the total number of VIN3 proteins in the yellow line from the detected number of VIN3-SYFP2 proteins. This factor can be estimated by taking the ratio of mRNA expression levels of *VIN3* to *SYFP2*, then normalising this by the ratio of *VIN3* to *GFP* expression in the green line, which lacks endogenous *VIN3*. The error in the correction factor is propagated directly from the s.e.m. of the independent measurements in panels A-B. Given the uniform rate of increase of VIN3 expression in all lines regardless of labelling, the correction factor is expected to be constant over time. Taking an inverse-variance-weighted average over the three timepoints, the correction factor used in this work is 2.0 ± 0.7, which is consistent with the expected genotype of the yellow line: a single exogenous gene copy of *VIN3-SYFP2* and a single native gene copy of *VIN3*.

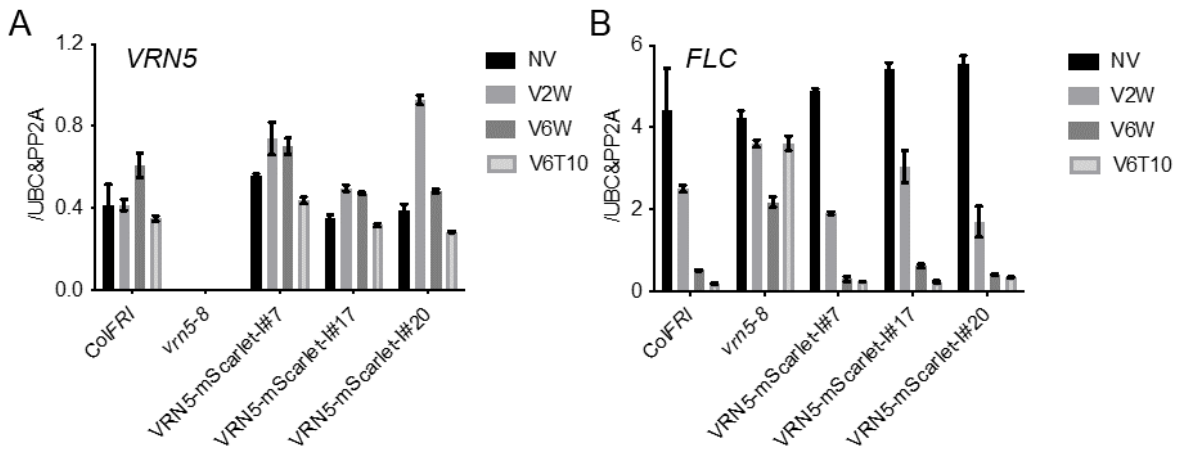

Supplementary Fig. 6. RNA expression analysis of *VRN5* and *FLC* in single-colour VRN5-mScarlet-I lines. Expression level of *VRN5* (A), of spliced *FLC* (B) in VRN5-mScarlet-I, *vrn5-8* and Col*FRI* seedlings before (NV) and after 2 weeks and 6 weeks cold treatments (V2W, V6W). V6T10 represents 10 days after a 6 week-cold treatment. Data are presented as mean ± s.d. (N=3) from 1 biological experiment. The samples of VRN5-mScarlet-I are from heterozygous T2 seedlings.

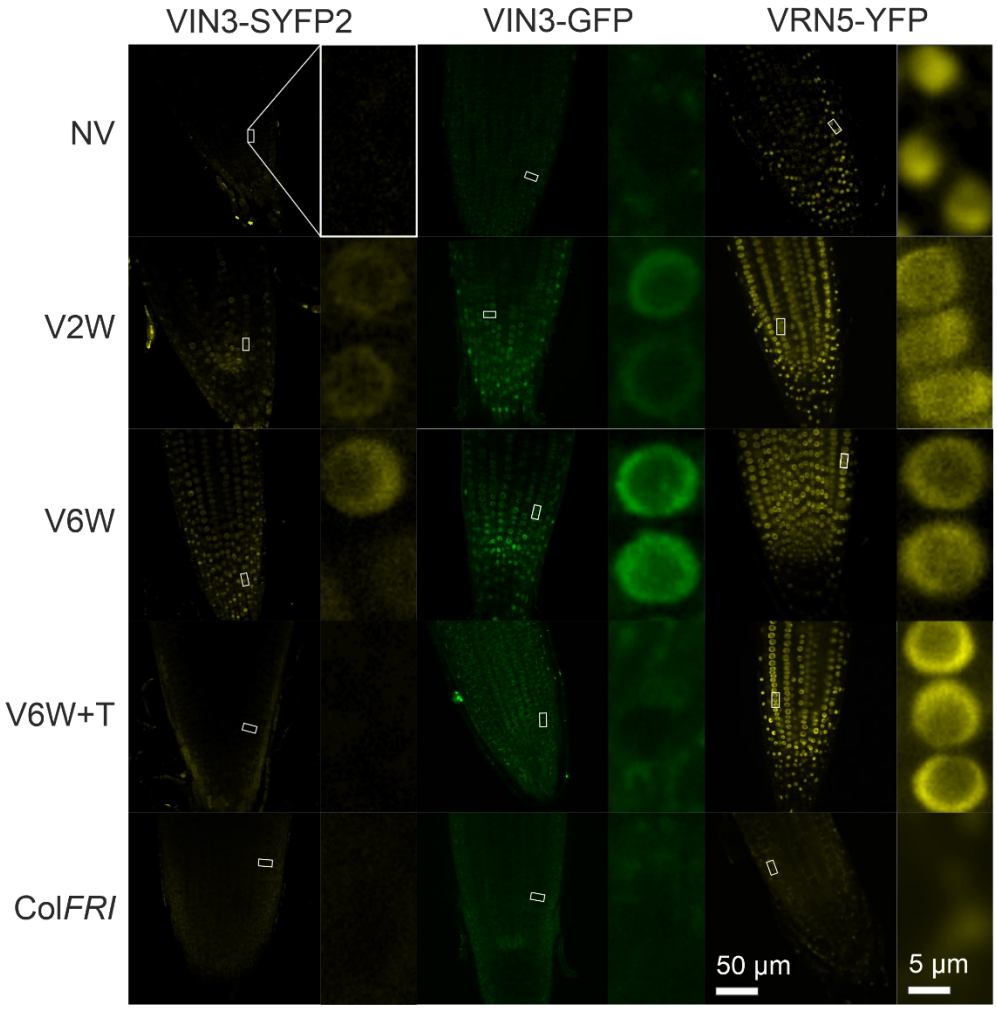

Supplementary Fig. 7. Confocal microscopy indicates VIN3 and VRN5 expression increase due to vernalisation.

Confocal microscopy projections of live whole root tips of VIN3-GFP and VRN5-YFP at different timepoints. NV is non-vernalised; V2W and V6W refers to 2 or 6 weeks of cold respectively; the post-vernalised timepoint V6W+T refers to 7 days warm (V6W+T7) for VIN3 and 14 days warm (V6W+T14) for VRN5. Bright particles outside the root envelope are remnants of the root cap. Also shown are insets at 13× scale to show detail of the labelled protein signals, which are consistently localised to the nucleoplasm, but not the nucleolus of each cell.

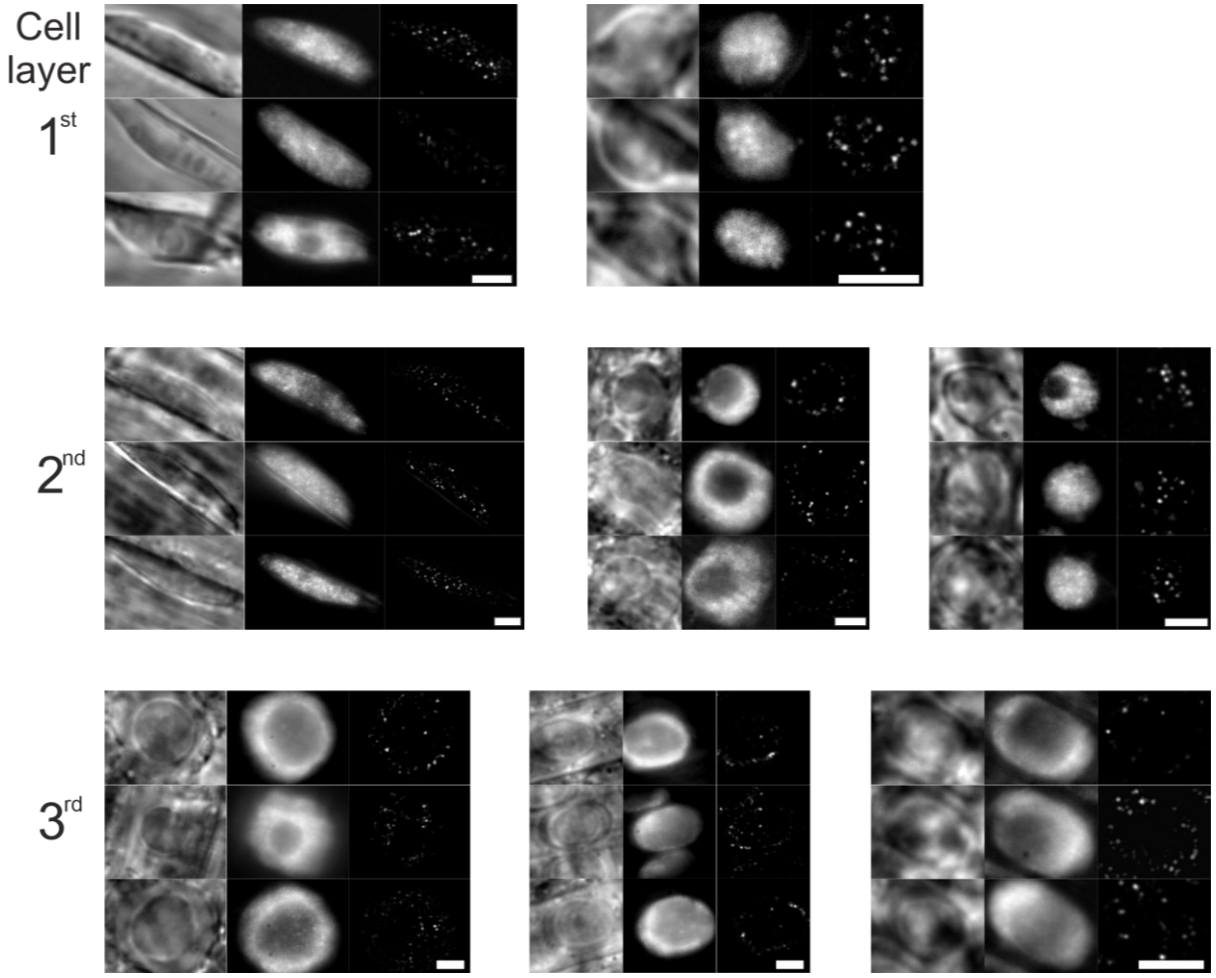

Supplementary Fig. 8. SlimVar detects molecular assemblies with high contrast across at least 3 cell layers in a range of cell morphologies.

SlimVar images of individual nuclei in the VRN5-YFP line, classified qualitatively by cell shape and location in root tip. Three independent fields of view (rows) are shown for each class at a mixture of timepoints before, during and after vernalisation. Left: brightfield, centre: initial fluorescence in SlimVar (average of first 3 frames); right: assemblies revealed by partial photobleaching during SlimVar sequence; visualisation generated in ImageJ from raw sequences by Gaussian smoothing at 1.0 pixel radius, gamma transform of 1.25, background subtraction at 10 pixel radius, followed by maximum projection over frames 30–100 in each sequence, then repeat background subtraction and Gaussian smoothing, then inverse gamma transform of 0.80. Exposure time: 10-20 ms. Scale bars: 10 µm.

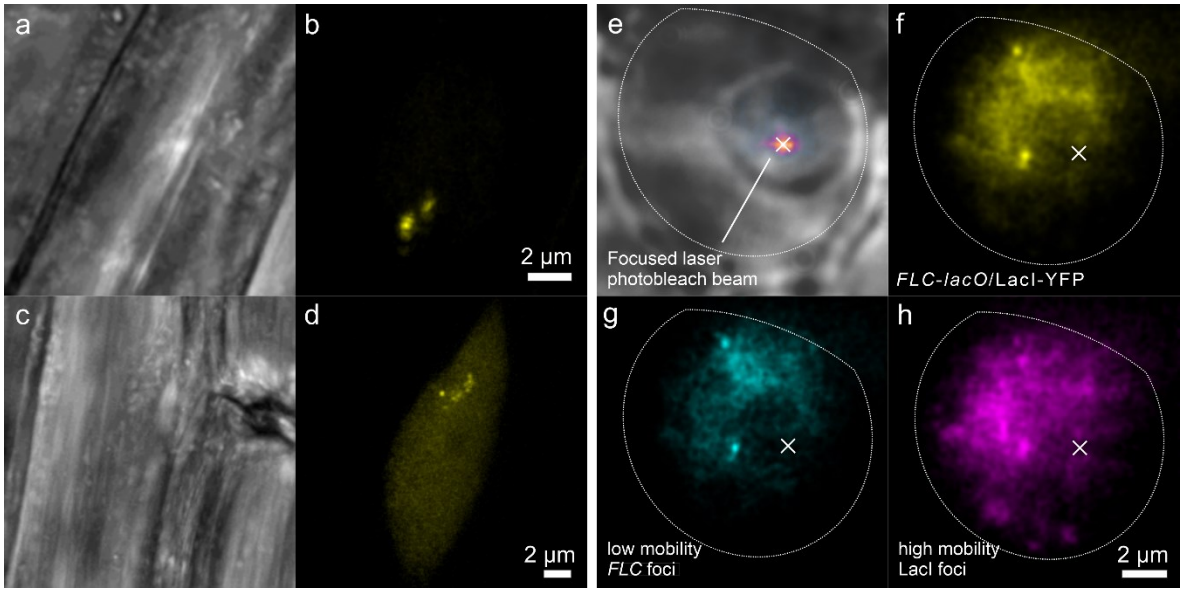

Supplementary Fig. 9. Confocal and SlimVar imaging of the FLC-*lacO*/LacI-YFP line. a-d) Confocal: a) Transmission and b) confocal fluorescence imaging of an non-vernalised nucleus in the epidermal meristem showing at least 2 loci, and c,d) a vernalised (six weeks of cold) nucleus in the epidermal elongation zone, featuring additional clustered pairs of *FLC* foci consistent with endoreduplication. Mobile LacI-YFP form a uniform background due to motion blur. Scale bars 2 µm. e-h) SlimVar: e) a large nucleus (dotted outline) of a non-vernalised cortical cell imaged in brightfield with superposed intensity profile of a focused laser beam (cross) inside the nucleolus; an initial exposure with this beam, typically 30 s, removes excess unbound LacI-YFP that diffuses through the excitation volume, while preserving any bound to the *lacO* array at the *FLC* transgene; f-h) the subsequent SlimVar acquisition shown as f) mean average, g) median projection showing isolated and low mobility *FLC* foci at the expected frequency of ≥2 loci per nucleus, whose diffusivity is quantified and used to match the diffusivity of VIN3 and VRN5 proteins of interest under the same acquisition conditions (Supplementary Table 1); and h) standard deviation projection indicating residual fast-moving LacI-YFP. In spot-bleached nuclei, we find a mean of 4.4 ± 0.8 slow LacI-YFP tracks per nucleus (N=38 nuclei) reflecting the expected two *FLC* transgenes plus a minority of endoreduplication loci. At the observed particle number density, the likelihood of random overlap of more than two free LacI-YFP tetramers is extremely low. We therefore identify all LacI-YFP tracks with stoichiometry greater than three tetramers, or a threshold of 12 LacI-YFP, as potential *FLC* loci. These tracks exhibit a diffusivity (Fig. 6a) of D_{FLC} = 0.20 ± 0.02 $\mu m^2 s^{-1}$ (N=129, mean ± s.e.m., 20 ms exposure). Tracks in the upper quartile of LacI-YFP stoichiometry (>81 LacI-YFP molecules), corresponding to the brightest foci per nucleus, yield an equivalent diffusivity estimate of 0.17 ± 0.04 $\mu m^2 s^{-1}$ (N=36; p= 0.097 |ns). With or without pre-bleaching, tracks with fewer than 12 LacI-YFP molecules typically diffuse faster, around 0.54 ± 0.04 $\mu m^2 s^{-1}$ (N=153; p= 0.0094 |*), which suggests they may consist of free LacI tetramers.

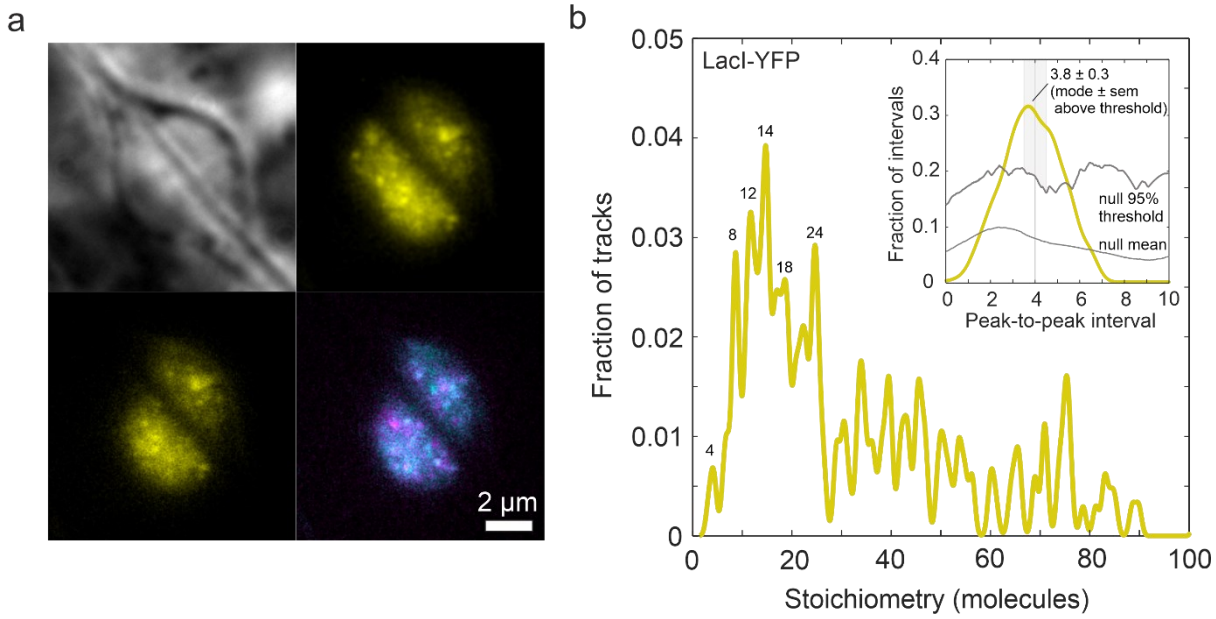

Supplementary Fig. 10. Tetrameric spacing of LacI-YFP validates peak interval extraction from stoichiometry distributions. a) Representative SlimVar images of neighbouring epidermal nuclei before vernalisation in single-colour *FLC-lacO*/LacI-YFP line under strong EtOH induction, shown as brightfield, initial SlimVar frame, and projections of mean (yellow), and merged median (cyan) and standard deviation (magenta) respectively over 5 frames. b) The stoichiometry of detected LacI-YFP tracks (n=225) shows clear peaks at approximate multiples of 4, with occasional interceding multiples of 2, consistent with the tightly bound tetrameric (dimer-of-dimer) complex of LacI. The maximum stoichiometry observed is 380 molecules (not shown for clarity). Inset: the most common spacing between neighbouring peaks in the stoichiometry distribution as estimated by the new method. The threshold above which the null distribution can be rejected is the 95th percentile fraction of intervals (grey trace) output from simulated random stoichiometry (Methods). The most common interval is given by the modal peak value above the null threshold (3.8 ± 0.3 molecules), which is consistent only with integer 4 molecules, and thus a tetrameric repeat unit as expected.

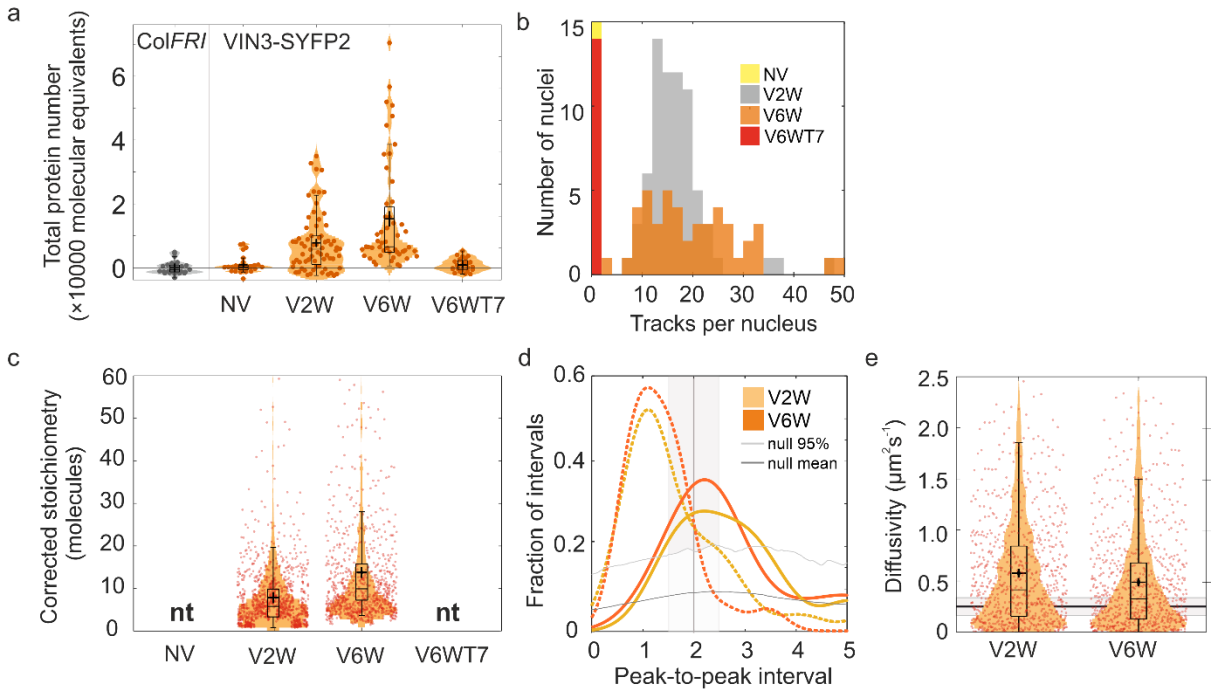

Supplementary Fig. 11. Collated SlimVar observations of VIN3-SYFP2. a) Distributions of integrated nuclear intensity of VIN3-SYFP2 in individual nuclei before, during and after vernalisation. NV = not vernalised; V2W = two weeks of cold; V6W = six weeks of cold; V6WT7 = six weeks of cold followed by one week of warm conditions. In the VIN3-SYFP2 line, the unlabelled, endogenous fraction of VIN3 protein can be accounted for by a factor of 2.0 ± 0.7 derived from the relative mRNA expression levels (Supplementary Fig. 5). Bar, box and whisker denote median, interquartile range (IQR) and 1.5× IQR respectively; cross: mean ± s.e.m. Total protein numbers of VIN3-SYFP2 range from negligible before cold (410 ± 560 molecules, BM test vs. Col*FRI*, N=52, p= 0.52 |ns), through 7,800 ± 1,600 molecules above background at 2 weeks cold (N=68, p<0.001|**) up to a peak of 15,000 ± 3,000 molecules at 6 weeks cold (N=51, p=0.0045|*). At 7 days after transfer to warm, the number of VIN3-SYFP2 again drops to a negligible amount (900 ± 700 molecules per nucleus, BM test vs. Col*FRI*, N=54, p=0.08|ns). b) The mean number of VIN3 tracks per nucleus cannot be distinguished between VIN3-SYFP2 and VIN3-GFP, nor does this change significantly between 2 and 6 weeks' vernalisation in either case (V2W: 16.3 ± 1.0 and 18.3 ± 1.9, N=120, p=0.42|ns; V6W: 17.4 ± 2.4 and 17.9 ± 1.8, N=140, p=0.22|ns respectively). c) After accounting for unlabelled VIN3, the mean labelled stoichiometry increases from 7.8 ± 2.7 molecules at 2 weeks' cold to 13.8 ± 3.9 at 6 weeks' cold (N=1792 tracks, p<0.001). d) The stoichiometry distribution for VIN3-SYFP2 has a smaller periodicity (dashed lines), which is incompatible with an integer number of molecules greater than one. However, after accounting for unlabelled VIN3, the resulting periodicity (2.2 ± 0.8, V2W; 2.2 ± 0.8, V6W, solid lines) is also consistent with dimeric subunits in VIN3 assemblies during vernalisation.

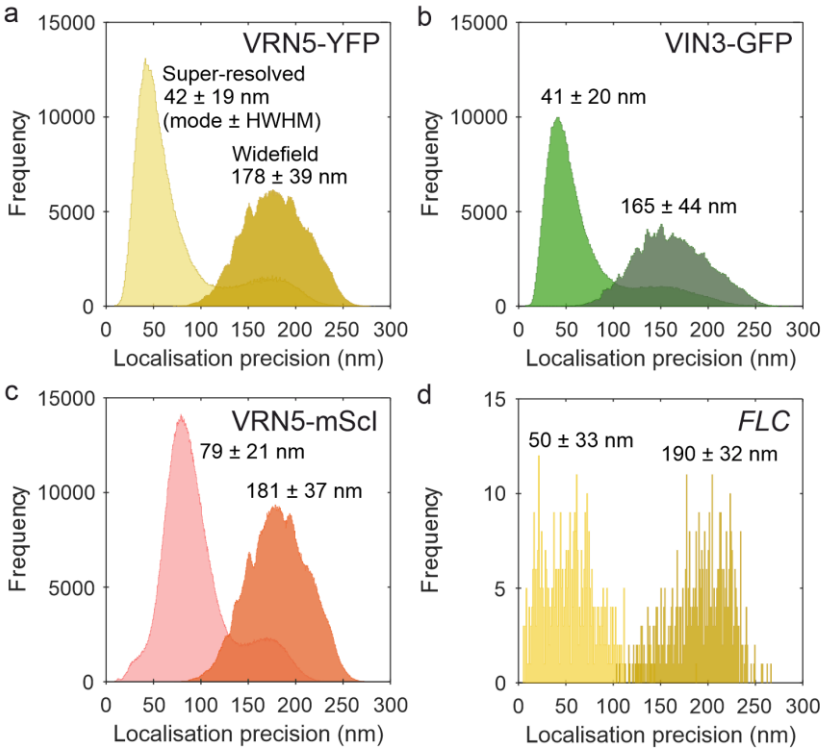

Supplementary Fig. 12. Localisation precision of tracked fluorescent foci in SlimVar acquisitions. Gaussian-fit widefield FWHM (major axis) and the corresponding super-resolved localisation precision estimated using the formulation of Thompson et al. [93] for foci within a) VRN5-YFP tracks (n= 5326), b) VIN3-GFP tracks (n=2479) at 2 ms exposure per frame; c) VRN5-mScI tracks (n=6395) and d) *FLC-lacO*/LacI-YFP loci (n=475) at 20 ms exposure. The localisation precision becomes finer with greater photon counts in each focus. However, most localisations occur during later stages of photobleaching; these are relatively dim compared to background counts, and therefore do not reach the theoretical limit scaling as the inverse square root of the photon count. For the brightest foci, we observe values smaller than the lateral spatial localisation precision for a single molecule (40 nm) but these should be interpreted with caution since the physical size of each assembly is unknown.

Supplementary Video legends

Supplementary Video 1. SlimVar resolves dynamic VRN5-YFP assemblies in live root tips. A single nuclear acquisition of VRN5-YFP line in an epidermal cell (10 µm deep) at non-vernalised (NV) conditions showing distinct assemblies. Left: raw data; right: photobleach corrected and Gaussian smoothed by 1 pixel width to emphasise dynamic assemblies. Scale bar: 1 µm, frame duration 2 ms, frame rate 25 fps.

Supplementary Video 2. VRN5-YFP assemblies in live root tips after vernalisation.

1853 A SlimVar acquisition in a large cortical nucleus (25 µm deep) in the VRN5-YFP line at post-
1854 vernalised (V6WT14) conditions showing large assemblies. Left: raw data; right:
1855 photobleach corrected and Gaussian smoothed by 1 pixel width. Scale bar: 2 µm, frame
1856 duration 20 ms, frame rate 10 fps.

1857 **Supplementary Video 3. VIN3-GFP assemblies during vernalisation.**

1858 A representative SlimVar acquisition of a smaller epidermal nucleus in VIN3-GFP line at 2
1859 weeks' cold. VIN3 has significantly lower copy number and stoichiometry compared to
1860 VRN5, and background is higher in GFP channel relative to YFP. Scale bar 1 µm, frame
1861 duration 2 ms, frame rate 25 fps, as for Video 1.